




ARTICLE

Tissue-resident macrophages in omentum promote metastatic spread of ovarian cancer

Anders Etzerodt^{1,2} , Morgane Moulin^{1,3}, Thomas Koed Doktor⁴, Marcello Delfini¹, Noushine Mossadegh-Keller¹, Marc Bajenoff¹ , Michael H. Sieweke^{1,5}, Søren Kragh Moestrup^{2,6}, Nathalie Auphan-Anezin¹ , and Toby Lawrence^{1,3,7} 

Experimental and clinical evidence suggests that tumor-associated macrophages (TAMs) play important roles in cancer progression. Here, we have characterized the ontogeny and function of TAM subsets in a mouse model of metastatic ovarian cancer that is representative for visceral peritoneal metastasis. We show that the omentum is a critical premetastatic niche for development of invasive disease in this model and define a unique subset of CD163⁺ Tim4⁺ resident omental macrophages responsible for metastatic spread of ovarian cancer cells. Transcriptomic analysis showed that resident CD163⁺ Tim4⁺ omental macrophages were phenotypically distinct and maintained their resident identity during tumor growth. Selective depletion of CD163⁺ Tim4⁺ macrophages in omentum using genetic and pharmacological tools prevented tumor progression and metastatic spread of disease. These studies describe a specific role for tissue-resident macrophages in the invasive progression of metastatic ovarian cancer. The molecular pathways of cross-talk between tissue-resident macrophages and disseminated cancer cells may represent new targets to prevent metastasis and disease recurrence.

Introduction

Macrophages populate all human tissues, and their involvement in tumor progression and metastasis is well documented (Noy and Pollard, 2014). Recent advances in our understanding of macrophage biology suggest that tissue-resident macrophages and infiltrating tumor-associated macrophages (TAMs) display a high degree of heterogeneity, in terms of both phenotype and ontogeny. However, our understanding of the physiological relevance of this heterogeneity and its implications for tumor development is still limited. In particular, the role of resident macrophages in tissue-specific tumor initiation and progression is unclear.

Ovarian cancer is the eighth leading cause of cancer-related death in women worldwide and has a particularly poor prognosis due to almost 80% of cases being diagnosed with late-stage invasive disease (Ferlay et al., 2018). In particular, high-grade serous ovarian carcinoma (HGSOC), the most frequent and aggressive form of ovarian cancer, is characterized by the formation of malignant ascites and peritoneal metastases, which results in a disastrous prognosis (Lengyel, 2010). HGSOC originates from transformation of fallopian tube or ovarian surface epithelial cells that disseminate at early stages into the

peritoneal cavity by exfoliation (Lengyel, 2010). Due to the lack of any anatomical barriers, exfoliated cancer cells are carried by the peritoneal fluid and spread throughout the abdominal cavity in a process termed transcoelomic metastasis (Kipps et al., 2013). Several reports have also suggested that ovarian cancer cells in ascites acquire cancer stem cell (CSC)-like properties that may play an important role in metastatic spread, chemosensitivity, and disease recurrence after therapy (Bapat et al., 2005). The most frequent site for metastasis in HGSOC is the omentum (Sehoul et al., 2009), an apron of visceral adipose tissue in the abdomen formed from a fold of the peritoneal mesothelium. Omentum contains a high density of lymphoid aggregates known as milky spots or fat-associated lymphoid clusters (FALCs), which are thought to contribute to peritoneal and intestinal immunity (Krist et al., 1995; Rangel-Moreno et al., 2009; Bénézech et al., 2015). The tropism of ovarian cancer cells for the omentum and its implications for disease progression are not yet fully understood. Several reports have suggested that FALCs play an active role in colonization of omentum (Hagiwara et al., 1993), but the tumor-promoting function of FALCs was shown to be independent of both B and T lymphocytes (Clark et al., 2013).

¹Aix Marseille Univ, CNRS, INSERM, CIML, Marseille, France; ²Department of Biomedicine, University of Aarhus, Aarhus, Denmark; ³Centre for Inflammation Biology and Cancer Immunology, School of Immunology & Microbial Sciences, King's College London, London, UK; ⁴Department of Biochemistry and Molecular Biology, University of Southern Denmark, Odense, Denmark; ⁵Centre for Regenerative Therapies, TU Dresden, Dresden, Germany; ⁶Institute of Molecular Medicine, University of Southern Denmark, Odense, Denmark; ⁷Henan Key Laboratory of Immunology and Targeted Therapy, School of Laboratory Medicine, Xinxiang Medical University, Xinxiang, China.

Correspondence to Toby Lawrence: toby.lawrence@kcl.ac.uk; Anders Etzerodt: ae@biomed.au.dk.

© 2020 Etzerodt et al. This article is distributed under the terms of an Attribution–Noncommercial–Share Alike–No Mirror Sites license for the first six months after the publication date (see <http://www.rupress.org/terms/>). After six months it is available under a Creative Commons License (Attribution–Noncommercial–Share Alike 4.0 International license, as described at <https://creativecommons.org/licenses/by-nc-sa/4.0/>).

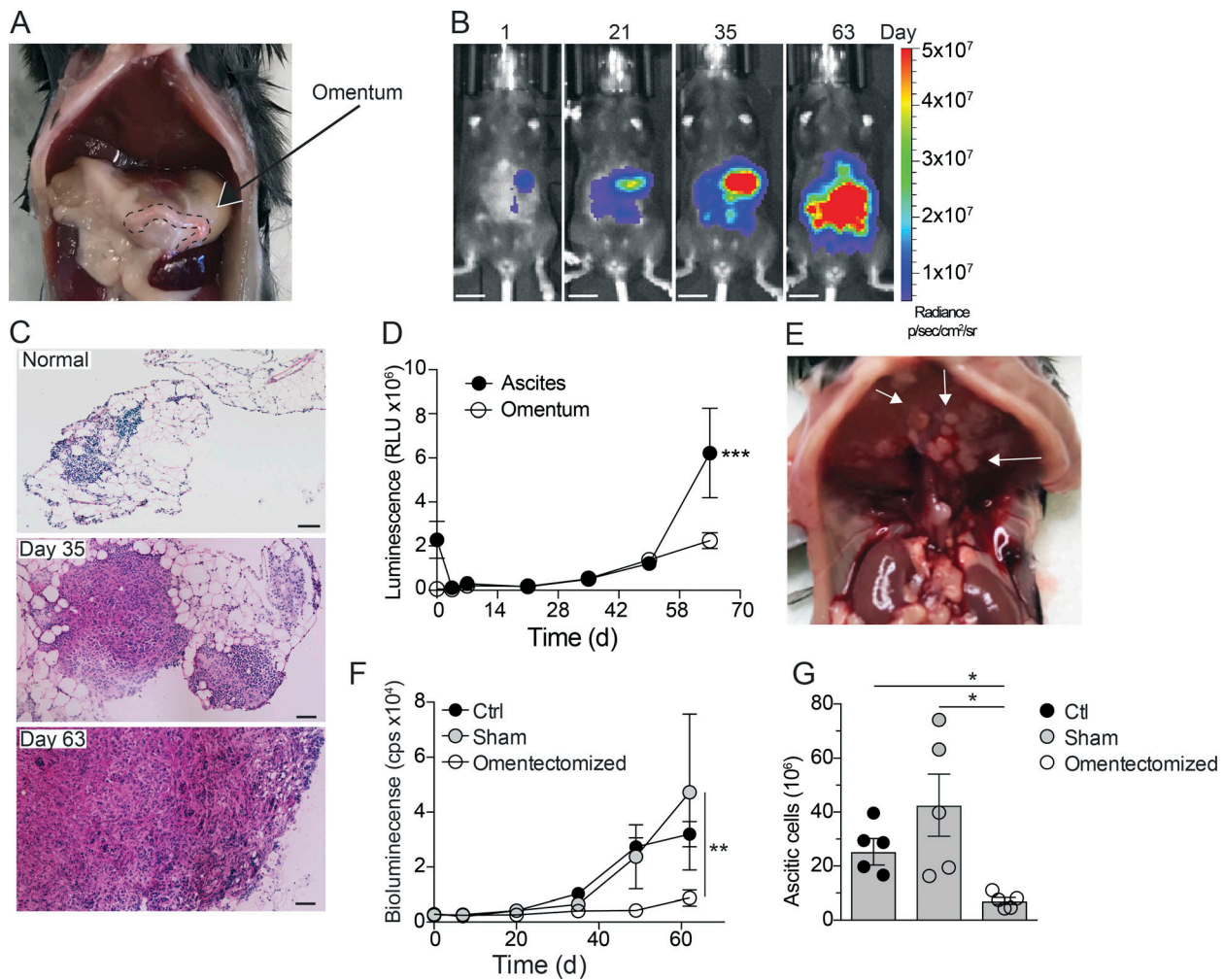


Figure 1. Omentum is a critical premetastatic niche for ovarian cancer cells. (A) Location of the omentum in the abdominal cavity of mice. (B) In vivo bioluminescence imaging of mice at 1, 21, 35, and 63 d after i.p. injection of 10^6 ID8-Luc cells; scale bar: 1 cm. (C) H&E stain of frozen omental sections from naive mice or 35 and 63 d after injection of ID8-Luc cells; scale bar: 100 μ m. (D) Ex vivo luminescence analysis of omentum and ascites. RLU, relative luminescent unit. Data are represented as mean \pm SEM of $n = 5$, and statistically significant difference was calculated using two-way ANOVA followed by Tukey post hoc test; ***, $P < 0.001$. (E) Tumor nodules on the diaphragm of mice 10 wk after injection of ID8-Luc cells. (F) In vivo bioluminescence analysis of omentectomized, sham-operated, or control (Ctrl) mice from 0–63 d after injection of ID8-Luc cells. cps, counts per second. Data are represented as mean \pm SEM of $n = 5$, and statistically significant difference was calculated using two-way ANOVA followed by Tukey post hoc test; **, $P < 0.01$. (G) End-point analysis of malignant ascites in omentectomized or control mice 63 d after injection of ID8-Luc cells. Data are represented as mean \pm SEM of $n = 5$, and statistically significant difference was calculated using Kruskal-Wallis one-way ANOVA followed by Dunn’s multiple comparisons test; *, $P < 0.05$. All data are representative of two independent experiments.

Myeloid cells are also abundant in FALCs, and macrophage density was recently shown to increase proportionally with disease score in omenta from ovarian cancer patients (Pearce et al., 2018). However, the specific role of omental macrophages in colonization and disease progression remains to be explored.

Tissue-resident macrophages perform trophic functions that contribute to organ development, tissue remodeling, and homeostasis (Pollard, 2009). Experimental evidence has shown that TAMs contribute to tumor progression by promoting angiogenesis, matrix remodeling, and epithelial-to-mesenchymal transition (EMT; Raggi et al., 2016), which ultimately leads to increased cell invasion and metastasis (Noy and Pollard, 2014). These properties reflect the trophic functions of macrophages in development, and consistent with these developmental

functions, the transcriptome of TAMs from mammary gland tumors has been shown to be enriched for genes that also define embryonic macrophages (Ojalvo et al., 2010). Until recently, it was thought that tissue macrophages were maintained from bone marrow-derived monocyte precursors, with the exception of the brain microglia and Langerhans cells in the skin (Ginhoux et al., 2010; Ginhoux and Merad, 2010), and the same has generally been assumed for TAMs (Lahmar et al., 2016). However, recent advances in molecular techniques that allow the fate-mapping of macrophages in vivo have revealed that most tissue macrophages originate from embryonic precursors and can be maintained by local proliferation with little input from the bone marrow (Schulz et al., 2012). Subsequent studies have shown that tissue-resident macrophages of embryonic origin

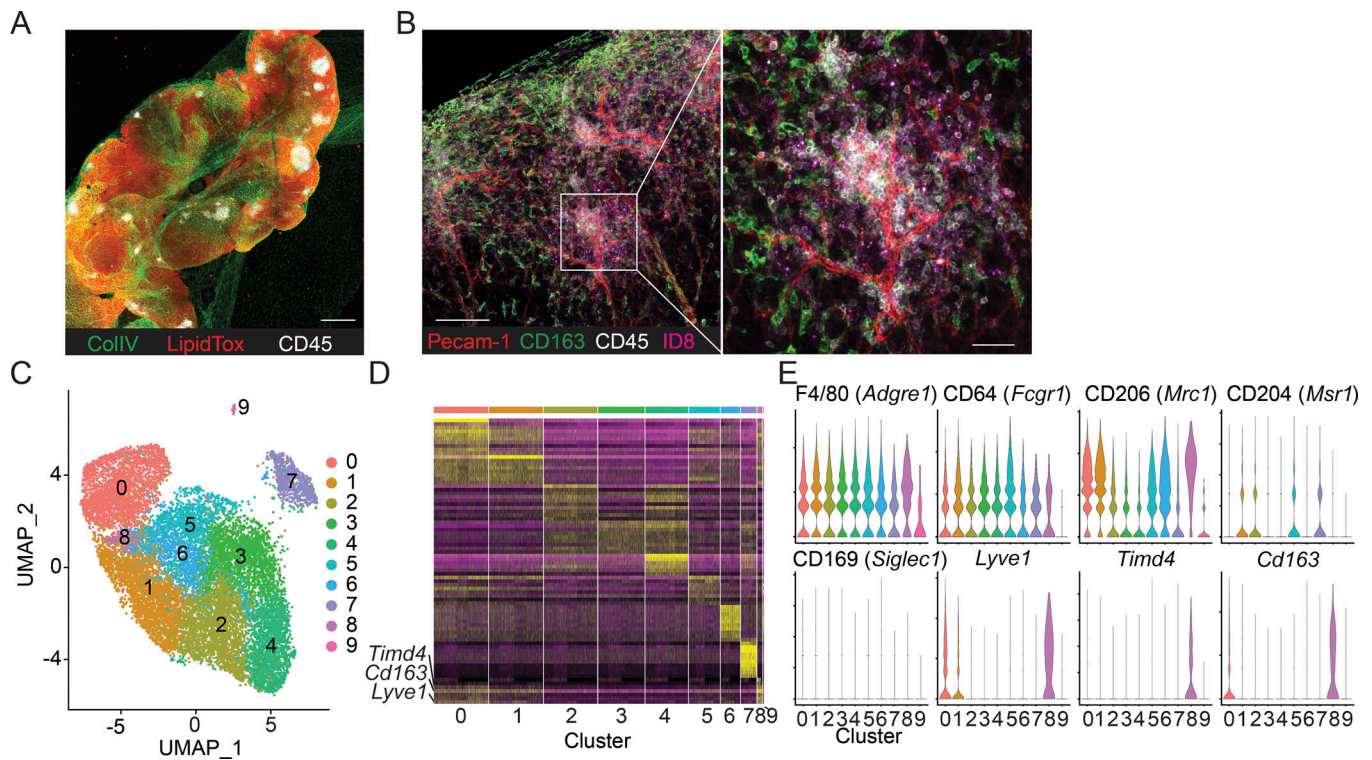


Figure 2. Single-cell transcriptional profiling of omental macrophages after tumor colonization. (A) Whole-mount confocal imaging of omentum showing the location of FALCs by visualizing collagen IV (CollIV, green), adipocytes (LipidTox, red), and leukocyte clusters (CD45, white); scale bar: 0.5 mm. (B) Whole-mount imaging of ID8-Luc infiltration in the omentum 24 h after injection of ID8 cells. Pecam-1 staining for blood vessels (red), CD163 for macrophages (green), CD45 for FALCs (white), and Qdot⁷⁰⁵ for ID8 cells (magenta); scale bar: 100 μ m and 50 μ m in magnification. (C) Two-dimensional representation and clustering of single-cell TAM transcriptomes using UMAP ($n = 16,514$). (D) Heatmap showing the top 10 DEGs in each UMAP cluster. (E) Violin plots showing expression of commonly used macrophage markers.

can be gradually replaced by monocyte-derived cells to varying degrees depending on the specific tissue (Ginhoux and Guilliams, 2016). The functional implications of these distinct developmental origins and their respective contributions to tumorigenesis have not yet been fully explored. However, recent reports suggest that embryo-derived tissue-resident macrophages can proliferate during tumor development and have distinct functions in tumor progression compared with monocyte-derived TAMs (Zhu et al., 2017; Loyher et al., 2018).

It is therefore critically important to further understand the specific axes of cross-talk between tissue-resident macrophages and cancer cells, during both tumor initiation and the malignant progression of disseminated tumor cells, as this may reveal new targets to combat tumor progression and thwart the development of invasive disease.

Here, we demonstrate that omentum represents a critical premetastatic niche in a mouse model of metastatic ovarian cancer and define a specific subset of tissue-resident macrophages in omentum that express CD163 and Tim4 and are required for the metastatic spread of ovarian cancer cells. Using genetic fate-mapping and shielded chimera experiments, we show that CD163⁺ Tim4⁺ omental macrophages are derived from embryonic progenitors and maintained independently of bone marrow-derived monocytes. Specific depletion of CD163⁺ Tim4⁺ macrophages, using genetic tools or antibody-targeted cytotoxic liposomes, was sufficient to prevent the development of

metastatic disease, whereas depletion of monocyte-derived TAMs had no impact. These studies suggest that specific interactions between disseminated tumor cells and tissue-resident CD163⁺ Tim4⁺ macrophages in the omentum promote the malignant progression of ovarian cancer. The molecular pathways that underly these interactions may represent new therapeutic targets for treatment of invasive metastatic disease.

Results

The omentum is a critical premetastatic niche for ovarian cancer cells

The omentum is an adipose tissue formed from a fold of the peritoneal mesothelium. In humans, the greater omentum covers the majority of the abdomen, whereas in mouse the omentum is only a thin stretch of adipose tissue located between the stomach, pancreas, and spleen (Fig. 1 A). The peritoneal spread of ovarian cancer has been modeled in mice using the immortalized mouse ovarian epithelial cell line ID8 (Roby et al., 2000). The i.p. injection of ID8 cells leads to the development of diffuse peritoneal carcinomatosis and malignant ascites with a long latency period (up to 12 wk), which has been widely used as a model of late-stage ovarian cancer (Charles et al., 2009; Motz et al., 2014; Lee et al., 2019). We used an ID8 cell line transduced to express firefly luciferase (ID8-luc; Hagemann et al., 2008) to monitor tumor progression after i.p. injection by noninvasive

bioluminescent imaging. We observed that ID8 cells localized primarily to the omentum for up to 35 d before spreading throughout the peritoneal cavity (Fig. 1 B). Infiltration of tumor cells into the omentum was confirmed by histological analysis, where visible tumor nodules could be observed within the adipose tissue from 35 d (Fig. 1 C). From day 63, the entire omentum was invaded by tumor cells, and only residual adipose tissue remained (Fig. 1 C). Interestingly, despite the presence of obvious tumor nodules in omentum from day 35, accumulation of ascitic ID8 cells was not detectable until >50 d after i.p. injection (Fig. 1 D). Ultimately, ascites formation was associated with the development of multiple distant metastases in the diaphragm and peritoneal wall (Fig. 1 E), reflecting late-stage disease in HGSOc patients. To establish the contribution of the omentum to the disease course in this model, we transplanted ID8-luc cells into omentectomized mice and monitored tumor growth. Whereas sham-operated and control mice showed a comparable course of tumor progression with accumulation of ascitic tumor cells after 63 d, we observed only minimal tumor growth in omentectomized mice, and ascitic cells were barely detectable (Fig. 1, F and G). These data suggested that the omentum was a critical premetastatic niche for tumor progression in this model and not merely a receptive site for peritoneal metastasis.

Ovarian cancer cells colonize FALCs in close contact with omental macrophages

The omentum has a particularly high density of FALCs, which are thought to be important structures for capturing peritoneal antigens (Rangel-Moreno et al., 2009; Fig. 2 A). Previous studies have proposed that FALCs promote the colonization of omentum by ovarian cancer cells; however, neither B or T lymphocytes were shown to contribute to tumor growth (Clark et al., 2013). To visualize the localization of ID8 cells in the omentum, we labeled the cells with Qdots (Qtracker705) before i.p. injection and analyzed omentum by whole-mount confocal imaging. 1 d after injection, we observed that ID8 cells were located in the vicinity of FALCs, an area densely populated by omental macrophages (Fig. 2 B). To further characterize omental macrophages after colonization with ID8 cells, we performed single-cell RNA sequencing (scRNAseq) on macrophages isolated from omentum 10 wk after injection of ID8 cells. Macrophages were isolated by flow-assisted cell sorting with gating on CD11b⁺ F4/80⁺ CD64⁺ cells and processed for scRNAseq analysis using the 10× Genomics Chromium platform. After filtering to exclude doublets and dead cells, we obtained 16,392 single-cell transcriptomes from four animals for downstream analysis. Uniform Manifold Approximation and Projection (UMAP) clustering analysis identified 10 major cell clusters (Fig. 2 C). Further analysis of the most significant differentially expressed genes (DEGs) in each cluster identified several common macrophage markers that were differentially expressed among these subsets. We identified a single cluster coexpressing *Lyve-1*, *Cd163*, and *Tim4* (Fig. 2, D and E), which have previously been used to characterize resident macrophages in various tissues. *Tim4* has been shown to be expressed by large peritoneal macrophages (Rosas et al., 2014), T cell zone macrophages in lymph nodes (Baratin et al., 2017), liver Kupffer cells (Scott

et al., 2016), and resident intestinal macrophages (De Schepper et al., 2018). *Lyve-1* was shown to be expressed by perivascular macrophages (Lim et al., 2018) and more recently by a subset of monocyte-derived interstitial macrophages in various tissues (Chakarov et al., 2019). Finally, *CD163* is expressed by a number of tissue-resident macrophage populations, including Kupffer cells, red pulp macrophages in the spleen, and bone marrow macrophages (Etzerodt and Moestrup, 2013). In addition to these three markers, several additional cell surface markers have been used to characterize tissue-resident macrophages. This includes *CD169* (Siglec-1) expression on bone marrow macrophages, alveolar macrophages, metallophilic macrophages in the spleen, and subcapsular sinus macrophages in the lymph nodes (Gray and Cyster, 2012). To further characterize the heterogeneity of omental macrophages, we analyzed the expression of these markers by flow cytometry. Gating on the CD11b⁺ myeloid cell fraction (CD45.2⁺ Lin⁻ [CD5, CD19, NK1.1, Ly6G, SiglecF]), we identified macrophages as F4/80⁺ CD64⁺ cells (Fig. 3 A, i), whereas monocytes were F4/80⁻ CD64⁻ CCR2⁺ (Fig. 3 A, ii). We observed a gradient of *CD169* expression, where only CD169^{hi} cells coexpressed *Lyve-1* (Fig. 3 A, iii). Further analysis showed that CD169⁻ *Lyve-1*⁻ and CD169^{int} *Lyve-1*⁻ cells were also negative for *CD163* and *Tim4* expression (Fig. S1 B), indicating a less mature phenotype. In contrast, CD169^{hi} *Lyve-1*⁺ cells could be separated into four distinct populations based on *CD163* and *Tim4* expression: CD163⁺ *Tim4*⁺ (P1), CD163⁺ *Tim4*⁻ (P2), CD163⁻ *Tim4*⁻ (P3), and CD163⁻ *Tim4*⁺ (P4; Fig. 3 A, iv). This analysis corroborated the UMAP clustering analysis on omental TAMs, where P1 macrophages represent cluster 8, and P2 macrophages represent cluster 0 (Fig. 2, C-E). In contrast, *Lyve-1*⁻ P3 and *Lyve-1*⁺ *Tim4*⁺ P4 macrophages were not separated based on the UMAP analysis.

We next analyzed the localization of these macrophage subsets in omentum by whole-mount confocal imaging. We found that CD169⁺ cells were distributed evenly throughout the tissue, whereas CD169⁺ CD163⁺ cells were located at the interface between FALCs and the surrounding adipose tissue (Fig. 3 B). *Tim4*⁺ CD163⁻ cells were mainly located within FALCs, whereas CD163⁺ *Tim4*⁺ cells were found only at the interface between FALCs and the surrounding adipose tissue (Fig. 3 C), similarly to CD169⁺ CD163⁺ cells (Fig. 3 B). Therefore, P1 (CD163⁺ *Tim4*⁺) and P2 (CD163⁺ *Tim4*⁻) macrophages are specifically located in the tissue surrounding FALCs, whereas P3 (CD163⁻ *Tim4*⁻) macrophages are widely distributed throughout the adipose tissue, and P4 (CD163⁻ *Tim4*⁺) macrophages appear to be located within FALCs.

To determine the dynamics of these macrophage subsets during colonization of omentum by ovarian cancer cells and tumor progression, we performed a kinetic analysis by flow cytometry after transplantation of ID8 cells. Among the CD11b⁺ myeloid fraction, CCR2⁺ monocytes represent the most abundant population in naive omentum, which remained unchanged for up to 4 wk after ID8 cell injection (Fig. 3 D). After 4 wk, the proportion of monocytes decreased coincidentally with an increase in CD169^{lo} *Lyve-1*⁻ macrophages, followed by a proportional increase in both CD169^{lo} *Lyve-1*⁻ and CD169^{int} *Lyve-1*⁻ and

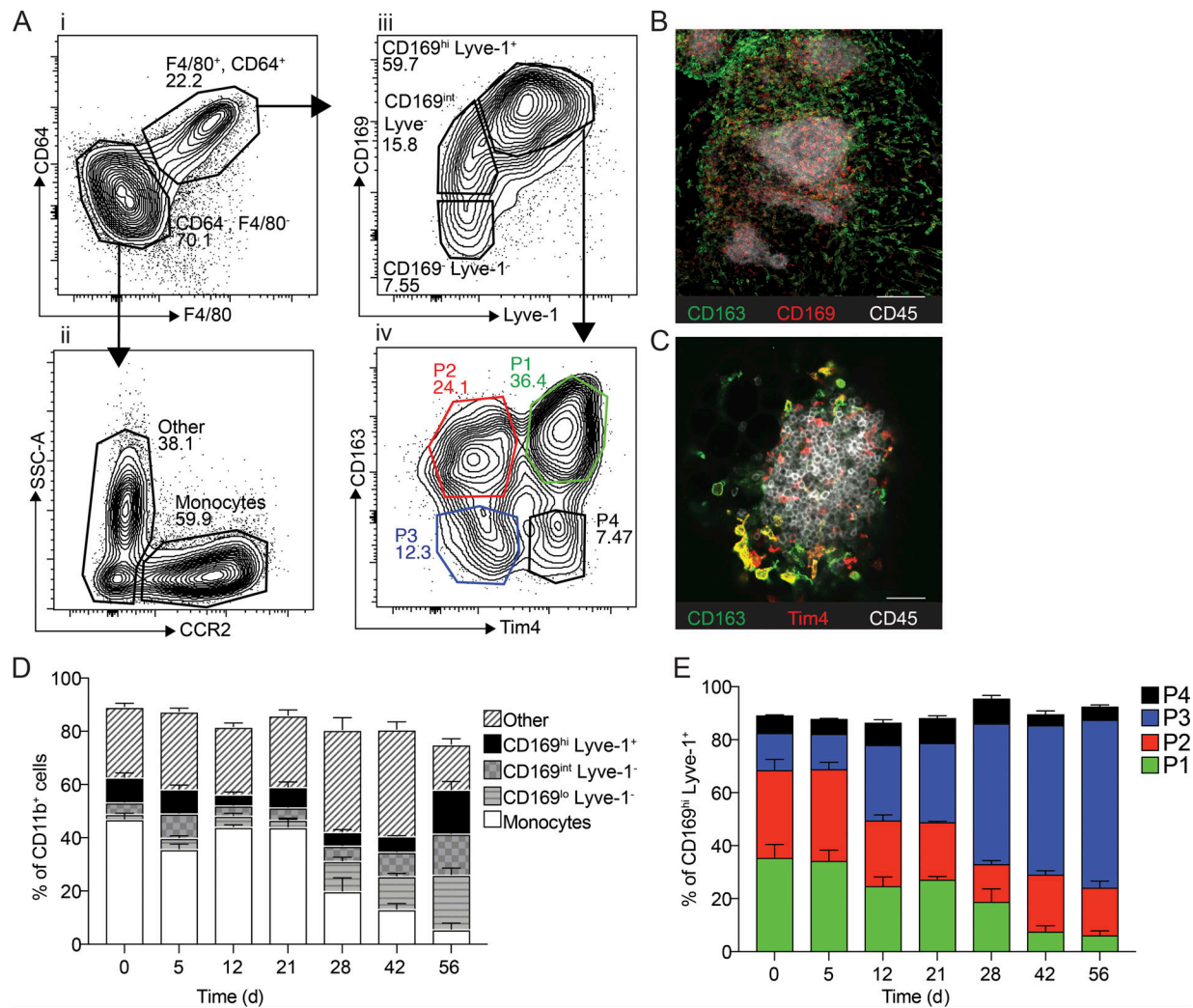


Figure 3. Characterization of macrophage subsets in omentum by flow cytometry and confocal microscopy. (A) Flow cytometry analysis of the myeloid cell compartment in omentum. Myeloid cells are gated as (i) Live, CD45.2⁺, singlets, Lin^{neg} (CD5, CD19, NK1.1, Ly6G, Siglec F), CD11b⁺, and subsequently macrophages were gated as F4/80⁺, CD64⁺. Monocytes were gated as (ii) F4/80⁻, CD64⁺, CCR2⁺. F4/80⁻, CD64⁻, and CCR2⁻ CD11b⁺ myeloid cells were designated as other. F4/80⁺ CD64⁺ macrophages were further gated based on (iii) CD169 and Lyve-1 expression, and finally CD169^{hi} Lyve-1⁺ cells were further divided into four subpopulations based on (iv) CD163 and Tim4 expression. SSC-A, side scatter area. (B) Whole-mount imaging of FALCs (CD45, white; CD169⁺, red; CD163⁺, green) in the omentum; scale bar: 100 μ m. (C) Whole-mount imaging of FALCs (CD45, white; CD163⁺, green; Tim4⁺, red) in omentum; scale bar: 50 μ m. (D) Flow cytometry analysis and relative distribution of CD11b⁺ myeloid cell populations shown in A, i–iii during tumor growth. (E) Flow cytometry analysis and relative distribution of CD169^{hi} Lyve-1⁺ macrophage subsets shown in A, iv during tumor growth. Whole-mount confocal imaging analysis is representative of $n = 4$ in two independent experiments. Flow cytometric data are represented as mean \pm SEM of $n = 4$ and are representative of two independent experiments.

CD169^{hi} Lyve-1⁺ cells at 6 and 8 wk of tumor growth (Fig. 3 D). The proportional increase in CD169^{hi} Lyve-1⁺ macrophages appeared to be driven by an increase in P3 (CD163⁻ Tim4⁺). In contrast, the proportion of P1 (CD163⁺ Tim4⁺), and to a lesser extent P2 (CD163⁺ Tim4⁻), was significantly decreased compared with normal omentum, whereas P4 (CD163⁻ Tim4⁺) remained relatively unchanged (Fig. 3 E).

In summary, these studies showed that ID8 cells colonize the omentum in the vicinity of FALCs and juxtaposed to resident CD163⁺ Tim4⁺ macrophages. As tumors progressed, there was an increase in the proportion of CD169⁺ Lyve-1⁺ macrophages, but the fraction of resident CD163⁺ Tim4⁺ cells remained stable.

Embryonic origin of tissue-resident CD163⁺ Tim4⁺ macrophages in omentum

To evaluate the ontogeny and homeostasis of the different macrophage subsets in omentum during ID8 tumor development, we prepared protected radiation chimeras using CD45.1 congenic C57BL/6 recipient mice. The abdomen of mice was protected with lead shielding to avoid radiation-induced replacement of tissue-resident macrophages. Following irradiation, we adoptively transferred bone marrow cells from CD45.1 \times CD45.2 F1 mice (CD45.1/2), which allowed the distinction between host (CD45.1⁺) and donor cells (CD45.1⁺/CD45.2⁺) by flow cytometry (Fig. 4 A). 5 wk after the bone marrow transplantation, chimerism was confirmed in blood by flow cytometry

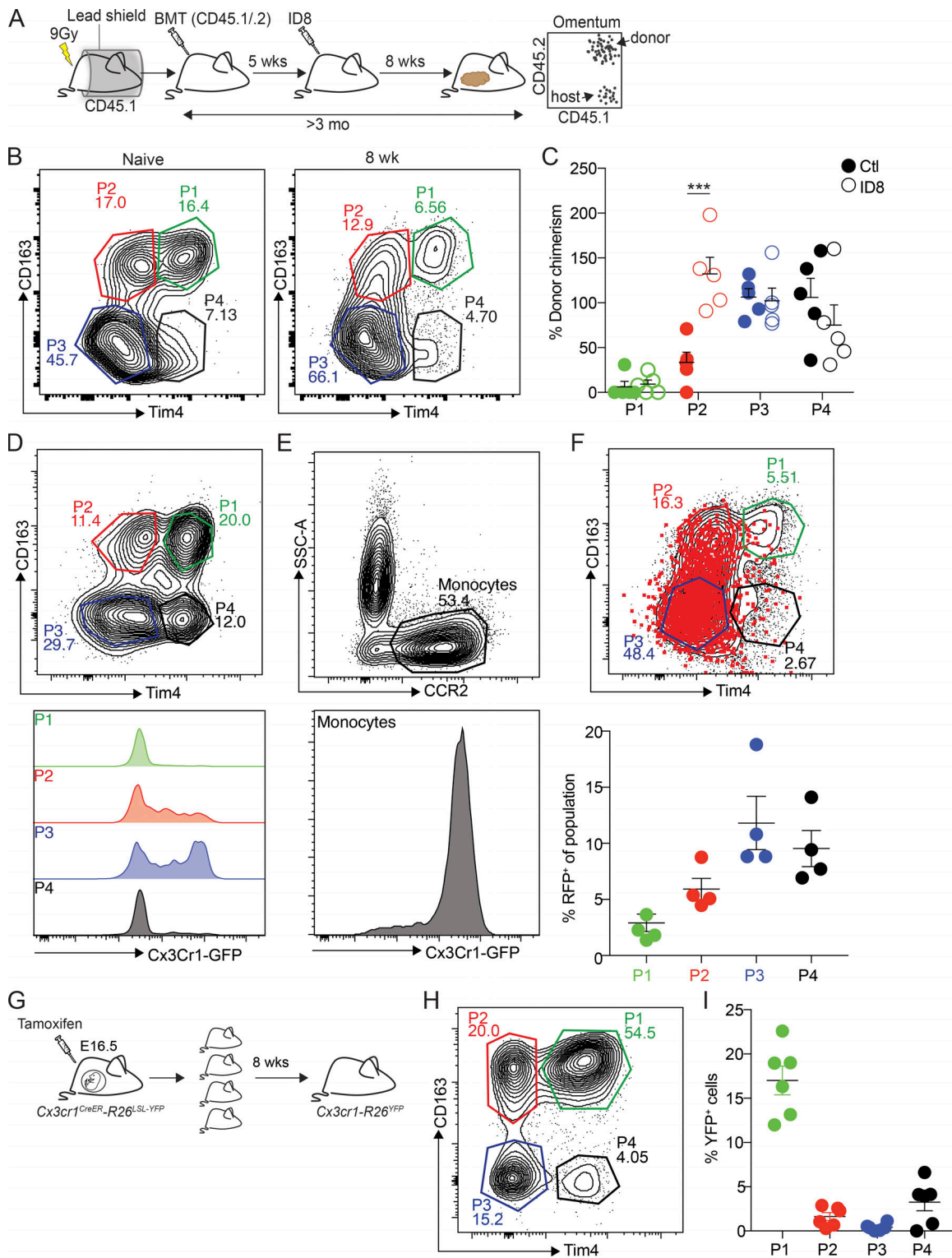


Figure 4. Embryonic origin of tissue-resident CD163⁺ Tim4⁺ macrophages in omentum. (A) Analysis of macrophage ontogeny in ID8 tumor-bearing mice using shielded chimeras; host CD45.1 congenic mice were placed in a protective lead shield with only the hind legs exposed, before irradiation at 9 Gy. The following day, mice were reconstituted with donor bone marrow cells from CD45.1/2 F1 mice. 5 wk after reconstitution, mice were injected with 10⁶ ID8-Luc cells i.p. At 8 wk after tumor injection, omentum was collected for analysis by flow cytometry. (B) Analysis of CD163 and Tim4 expression among CD169^{hi} Lyve-1⁺ macrophages in omentum from naive and tumor-bearing chimeric mice. (C) Chimerism was calculated as the proportion of CD45.1/2⁺ CD169^{hi} Lyve-1⁺ macrophages relative to CD45.1/2⁺ expression among Ly6C^{hi} blood monocytes. Data are represented as mean ± SEM of n = 5, and statistically significant difference was calculated using two-way ANOVA followed by Tukey post hoc test; ***, P < 0.001. (D and E) Flow cytometry analysis of Cx3Cr1-GFP expression in CD169^{hi} Lyve-1⁺ macrophages (P1–4; D) and CCR2⁺ monocytes (E). (F) Fate-mapping of Cx3Cr1-expressing monocytes in *Cx3cr1-R26^{dRFP}* mice inoculated with ID8-Luc cells. Mice were injected with ID8-Luc i.p., and after 8 wk, 1 mg of tamoxifen was administered by oral gavage, and RFP expression was analyzed in CD169^{hi}

Lyve-1⁺ macrophages 10 d later. Data are represented as mean \pm SEM of $n = 4$. **(G)** Analysis of CD169^{hi} Lyve-1⁺ macrophage ontogeny by pulse-labeling of Cx3Cr1-R26^{YFP} embryos with tamoxifen at E16.5. **(H)** Omentum was harvested and analyzed by flow cytometry 8 wk after birth. **(I)** The percentage of YFP⁺ cells was calculated relative to YFP⁺ microglia. Data are represented as mean \pm SEM of $n = 6$. All data are representative of two independent experiments.

(Fig. S2 A) before mice were injected with ID8 cells. After an additional 8 wk of tumor growth, omentum was harvested for analysis. To track bone marrow-derived cells, CD45.1 and CD45.2 expression by omental macrophages was analyzed and normalized to blood monocytes. Chimerism within P3 (CD163⁻ Tim4⁻) and P4 (CD163⁻ Tim4⁺) populations was, on average, close to 100%, in both naive and tumor-bearing mice (Fig. 4, B and C). In contrast, chimerism in P1 (CD163⁺ Tim4⁺) macrophages was close to zero, irrespective of tumor growth, while the P2 (Tim4⁻ CD163⁺) population showed ~40% chimerism in naive mice and complete chimerism in tumor-bearing mice (Fig. 4, B and C). These data showed that CD163⁺ Tim4⁺ omental macrophages (P1) were not replaced by bone marrow-derived cells throughout the course of this experiment, which was >3 mo. However, P3 and P4 cells were completely replaced in both steady state and during tumor development over this time course, suggesting that these cells represent monocyte-derived macrophages of limited life span. In contrast, CD163⁺ Tim4⁻ macrophages (P2) were only partially replaced over 3 mo at steady state, although they showed complete replacement during tumor growth. Therefore, these cells represent long-lived monocyte-derived macrophages whose replacement is accelerated during tumor development.

To verify the contribution of circulating monocytes to omental TAMs, we next performed a fluorescent fate-mapping experiment using mice expressing Cx3cr1-CreERT₂ (Cx3cr1^{CreER}) and a Rosa26-lox-STOP-lox(LSL)-tdRFP reporter allele (Cx3cr1-R26^{tdRFP}; Yona et al., 2013; Goossens et al., 2019). In adult mice, Cx3cr1 is expressed by monocytes in blood and omentum, but expression is decreased as monocytes mature into macrophages (Fig. 4, D and E). To label monocytes during tumor development, Cx3cr1-R26^{tdRFP} mice were injected with ID8 cells, and after 6 wk, mice were given a single dose of tamoxifen by oral gavage to activate RFP expression in Cx3cr1⁺ cells. 10 d later, RFP in omental macrophages was assessed by flow cytometry. As expected, P3 and P4 populations were most strongly labeled with RFP under these conditions, whereas P2 macrophages were labeled to a lesser extent (Fig. 4 F). In contrast, there was minimal labeling of CD163⁺ Tim4⁺ cells (P1; Fig. 4 F). These data are consistent with a rapid replacement of P3 and P4 macrophages by monocytes, while P2 cells are replaced with slightly slower kinetics. However, in keeping with data from shielded chimera experiments, there was very little replacement of P1 macrophages by Cx3Cr1-expressing precursors.

The experiments described above showed that CD163⁺ Tim4⁺ omental macrophages were not derived from bone marrow-dependent monocyte precursors, suggesting that these tissue-resident macrophages may be of embryonic origins. To evaluate the potential embryonic origins of these cells, we performed a fate mapping experiment with Cx3cr1^{CreER} mice in utero, since Cx3cr1 is expressed in both embryonic macrophage precursors and fetal monocytes (Yona et al., 2013). Cx3cr1-R26^{YFP} embryos

were pulse-labeled with tamoxifen at E16.5, and YFP expression in macrophages from omentum was subsequently analyzed by flow cytometry at 8 wk of age (Fig. 4 G). After normalization of YFP⁺ cells to microglia to assess labeling efficiency (Fig. S2 C), we observed that ~20% of P1 macrophages (CD163⁺ Tim4⁺) in adult omentum were YFP⁺ (Fig. 4, H and I), indicating an embryonic origin for these cells. In contrast, very few YFP⁺ cells were detected in the P2 (CD163⁺ Tim4⁻), P3 (CD163⁻ Tim4⁻), and P4 (CD163⁻ Tim4⁻) populations (Fig. 4, H and I), demonstrating that these cells were not derived from embryonic progenitors or were most likely replaced by monocyte-derived cells in the adult.

Collectively, these experiments show that CD163⁺ Tim4⁺ macrophages in omentum are uniquely independent of bone marrow-derived monocytes both in steady state and during tumor growth and are thus likely to maintain themselves locally by self-renewal. Furthermore, at least a significant proportion of these cells are of embryonic origin.

CD163⁺ Tim4⁺ tissue-resident macrophages express a unique transcriptional profile

To evaluate the impact of tumor growth on the phenotype of different macrophage subsets in omentum, we performed transcriptional profiling of cells sorted by flow cytometry at steady state and at different time points after seeding with tumor cells. We isolated P1, P2, and P3 macrophages by FACS from naive omentum and at 5 or 10 wk after injection of ID8 cells (Fig. 5 A) and prepared sequencing libraries directly from snap-frozen cell pellets. Libraries were sequenced to an average read depth of 42.7 million reads per sample. Unfortunately, the RNA yield in P4 macrophages was too low to generate sequencing libraries. A heatmap showing the 5,000 most-variable genes in the dataset is shown in Fig. S3 A. Initial analysis confirmed an overlap in the expression levels of the markers highlighted in the scRNAseq analysis; P1 macrophages coexpressing Lyve-1, CD163, and Tim4; and P2 macrophages expressing Lyve-1 and CD163, but not Tim4. However, P3 macrophages expressed very low levels of all three markers (Fig. S3 B). To analyze the relationship between the different macrophage populations, we performed a principal component analysis (PCA) combined with network analysis to show the n nearest neighbors. This analysis showed that the transcriptional profile of CD163⁺ Tim4⁺ resident macrophages (P1) did not undergo major changes during tumor growth, as all samples from this population clustered closely together (Fig. 5 B). Interestingly, the long-lived monocyte-derived CD163⁺ Tim4⁻ macrophages (P2) were closely related to CD163⁺ Tim4⁺ resident macrophages (P1) at steady state, but in tumor-bearing mice, they became more closely aligned to P3 (Fig. 5 B), which likely reflects the increased replacement of P2 macrophages by monocyte-derived cells during tumor growth (Fig. 4, B and C). To further analyze the transcriptional changes between these three major subsets in established tumors, we

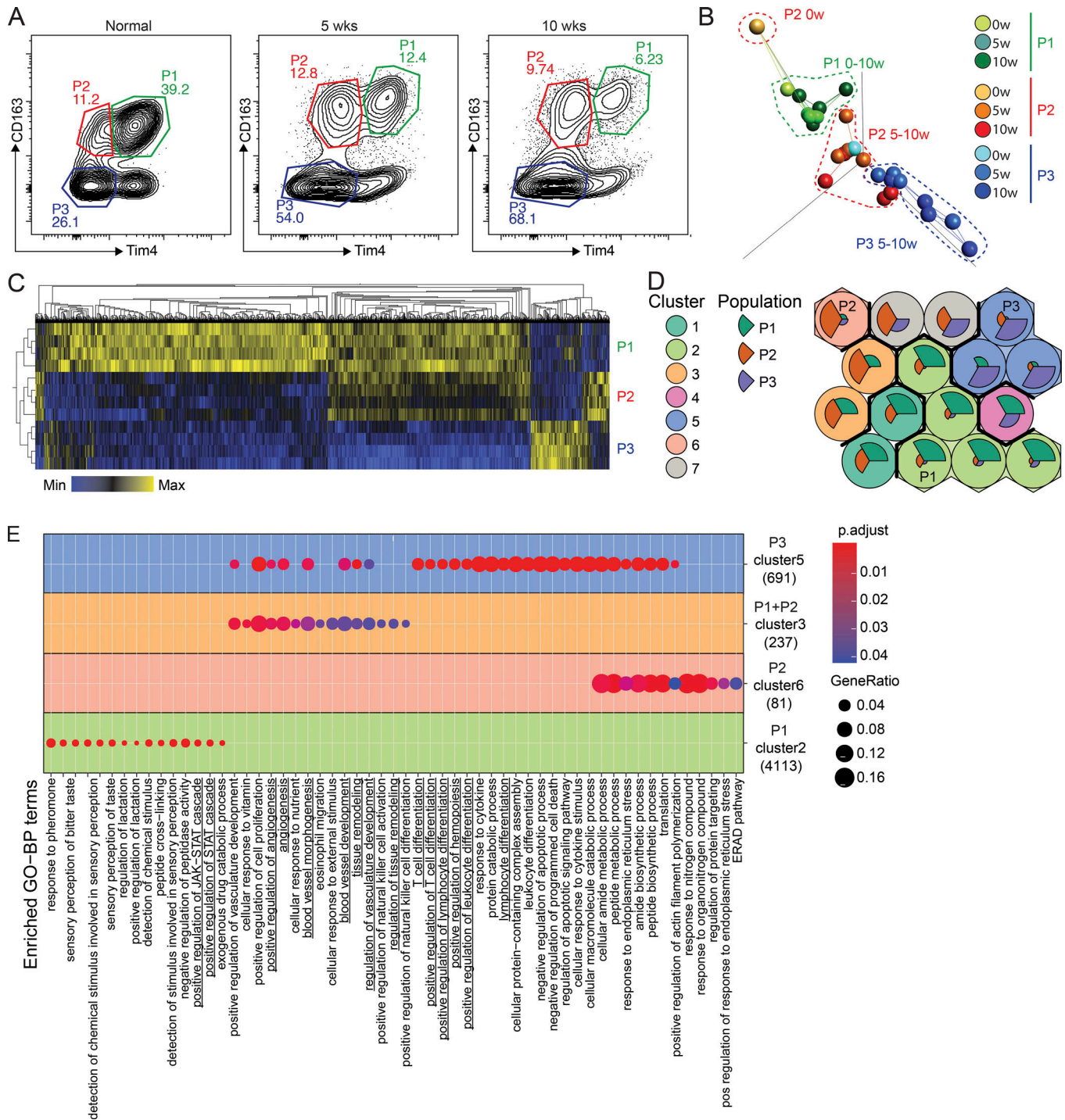


Figure 5. CD163⁺ Tim4⁺ tissue-resident macrophages express a unique transcriptional profile. (A) Gating strategy for cell sorting of P1, P2, and P3 populations of omental macrophages from naive ($n = 2$) and tumor-bearing mice at 5 and 10 wk after injection of ID8 cells ($n = 4$). 500 cells were sorted for each population and subjected to bulk RNAseq analysis. (B) PCA and network analysis of variable gene expression in P1, P2, and P3 macrophages. PCA analysis was performed on normalized data (mean = 0, and variance = 1), generating a correlation-based PCA plot. Network analysis connects k nearest neighbors ($k = 3$) based on similarity calculated by Pearson correlation. (C) Heatmap showing hierarchical clustering of the 5,000 most DEGs for each of the three populations at 10 wk of tumor growth. DEGs were identified by pairwise comparison with a cut-off of $P_{adjusted} > 0.01$. (D) SOMs of identified DEGs using the Kohonen package for R. The SOM analysis found 16 single SOMs that were subsequently grouped by hierarchical clustering to identify population-specific clusters (clusters 1–7). The magnitude of the pie slices indicates the relative proportions of genes enriched in P1 (green), P2 (brown), and P3 (blue) within the SOM. (E) ClusterProfiler enrichment analysis against the GO database on SOM clusters 1–7. Only clusters with significantly enriched pathways are visualized. Libraries were prepared from two independent experiments with $n = 2$ and sequenced on the same flow cell for a total of four biological replicates. ERAD, endoplasmic reticulum-associated protein degradation; pos, positive.

extracted DEGs by pairwise and grouped comparisons of P1, P2, and P3 at 10 wk of tumor growth (Fig. 5 C). We then performed a self-organizing map (SOM) clustering analysis to identify clusters of genes enriched in either a single population or a group of populations (Fig. 5 D). In the SOM clustering analysis, genes with a similar expression profile are first organized into SOMs. Within these maps, a pie chart depicts the relative enrichment of genes in the three populations analyzed (P1, P2, and P3), and the size of the pie slices reflects the gene enrichment. SOMs that are similar are then grouped together, generating clusters of SOMs with a comparable gene enrichment profile. This analysis generated 16 different SOMs that were subsequently grouped in 7 distinct clusters. Cluster 2 was enriched in P1, cluster 6 in P2, and cluster 5 in P3. Cluster 3 contained genes enriched in both P1 and P2, and cluster 7 was enriched in both P2 and P3. We then used ClusterProfiler enrichment analysis and the Gene Ontology (GO) database for the different SOM clusters to identify biological processes enriched in the different populations. This analysis revealed multiple enriched processes in clusters 2, 3, 5, and 6; the 15 most significant terms are shown in Fig. 5 E. Of particular interest, positive regulation of JAK-STAT signaling was uniquely enriched in CD163⁺ Tim4⁺ macrophages (P1, cluster 2; Fig. S5 A), whereas pathways related to angiogenesis, blood vessel development, and tissue remodeling were shared between CD163⁺ populations (P1 and P2, cluster 3; Fig. S5, B and C). Interestingly, the STAT pathway is part of the self-renewal gene regulatory network in macrophages (Soucie et al., 2016), in line with the ability of these cells to maintain themselves independently of bone marrow-derived monocytes. In addition, the pathways and processes enriched in both CD163⁺ populations (P1 and P2) have previously been linked with tumor-promoting functions of TAMs (Noy and Pollard, 2014). In contrast, pathways associated with T cell differentiation were uniquely associated with P3 (cluster 5; Fig. S5 D). This analysis suggested a functional diversification of omental macrophage subsets in the context of tumor growth.

Specific depletion of CD163⁺ Tim4⁺ macrophages prevents metastatic spread of ovarian cancer

Next, we sought to analyze the specific contributions of omental macrophage subsets to disease progression in our model. Initial experiments showed that tumor development and accumulation of malignant ascites were not affected in *Ccr2*^{-/-} mice (Fig. S4, A–D). These mice have impaired recruitment of monocyte-derived cells, suggesting a redundant function of CCR2-dependent monocyte-derived macrophages in disease progression. To assess the specific contribution of CD163⁺ Tim4⁺ tissue-resident macrophages (P1), we generated transgenic mice that exclusively express DTR in CD163⁺ macrophages (Cd163-Csf1r^{DTR}; Etzerodt et al., 2019); Cd163-iCre knock-in mice (Cd163^{iCre}) were crossed with transgenic mice expressing an LSL-DTR cassette under control of the Csf1r-promoter (Tg(Csf1r-LSL-DTR)). Flow cytometry analysis of omentum from Cd163-Csf1r^{DTR} mice 24 h after a single injection of diphtheria toxin (DT; 4 ng/kg) confirmed the specific ablation of CD163⁺ P1 and P2 macrophages (Fig. S4, E–G). However, 6 d after DT treatment, monocyte-derived P2 macrophages were

completely restored, while resident P1 macrophages remained absent (Fig. S4, E–G). In addition, there was also a complete recovery of CD163⁺ peritoneal macrophages 6 d after DT treatment (Fig. S4 H). Thus, this approach allows the selective ablation of resident CD163⁺ P1 macrophages in omentum and the opportunity to assess their unique contribution toward tumor progression. We treated cohorts of Cd163-Csf1r^{DTR} and Cre-negative littermate controls (Csf1r^{LSL-DTR}) with DT and 6 d later injected ID8 cells i.p. After 10 wk, omentum was collected for analysis by flow cytometry, and tumor progression was assessed (Fig. 6 A). At this time point, P1 macrophages remained depleted in omenta from Cd163-Csf1r^{DTR} mice while all other populations were unchanged (Fig. 6, B and C). Interestingly, although tumor seeding of the omentum was unaffected (Fig. 6 D), Cd163-Csf1r^{DTR} mice showed a significant reduction in ascitic tumor cells (Fig. 6 E) and reduced ascites (Fig. 6 F). Moreover, metastases to the diaphragm were significantly reduced in Cd163-Csf1r^{DTR} mice (Fig. 6, G and H). These data suggested that tissue-resident CD163⁺ Tim4⁺ macrophages in the omentum contributed significantly to the metastatic spread of ovarian cancer cells and the development of invasive disease.

To further substantiate the role of CD163⁺ macrophages in tumor progression, we used CD163-targeted cytotoxic lipid nanoparticles (LNPs) to therapeutically deplete CD163⁺ macrophages in tumor-bearing mice (Etzerodt et al., 2019). These LNPs contain 5% polyethylene glycol (PEG; molecular weight, 2,000 g/mol) in the lipid bilayer, which minimizes nonspecific phagocytic uptake, and are loaded with the cytotoxic drug doxorubicin (dxr) to kill target cells. LNPs are targeted specifically to CD163-expressing cells by conjugation of an anti-CD163 monoclonal antibody to PEG (Etzerodt et al., 2012). To achieve therapeutic depletion of CD163⁺ macrophages, mice were injected with ID8 cells and 5 wk later treated i.v. twice a week for 5 wk with vehicle, empty CD163-targeted LNPs (α CD163-ctrl), or dxr-loaded LNPs (α CD163-dxr; Fig. 6 I). In vivo bioluminescent imaging showed that continuous depletion of CD163⁺ cells after α CD163-dxr treatment resulted in a significant reduction of overall tumor burden in the abdomen (Fig. 6 J). As expected, sustained depletion of CD163⁺ cells led to the specific loss of both P1 and P2 macrophages in omentum (Fig. 6 K), which was accompanied by a significant decrease of tumor burden in both omentum and ascites (Fig. 6, L–N), suggesting that the additional absence of monocyte-derived CD163⁺ macrophages (P2) contributed to reduced tumor growth in the omentum (Fig. 6 L), which was not observed when only tissue-resident CD163⁺ Tim4⁺ macrophages (P1) were depleted (Fig. 6 D).

Ovarian cancer cells in ascites acquire CSC characteristics

Ascitic tumor development and peritoneal metastases indicate a particularly poor prognosis for ovarian cancer patients. Our studies showed a long latency in ascitic tumor development and peritoneal spread of ID8 cells after seeding the omentum, and omentectomy prevented development of ascitic disease (Fig. 1), suggesting that the omentum represents a key premetastatic niche. In addition, the studies described above showed that tissue-resident macrophages in omentum contributed significantly to the accumulation of ascitic cells and the development

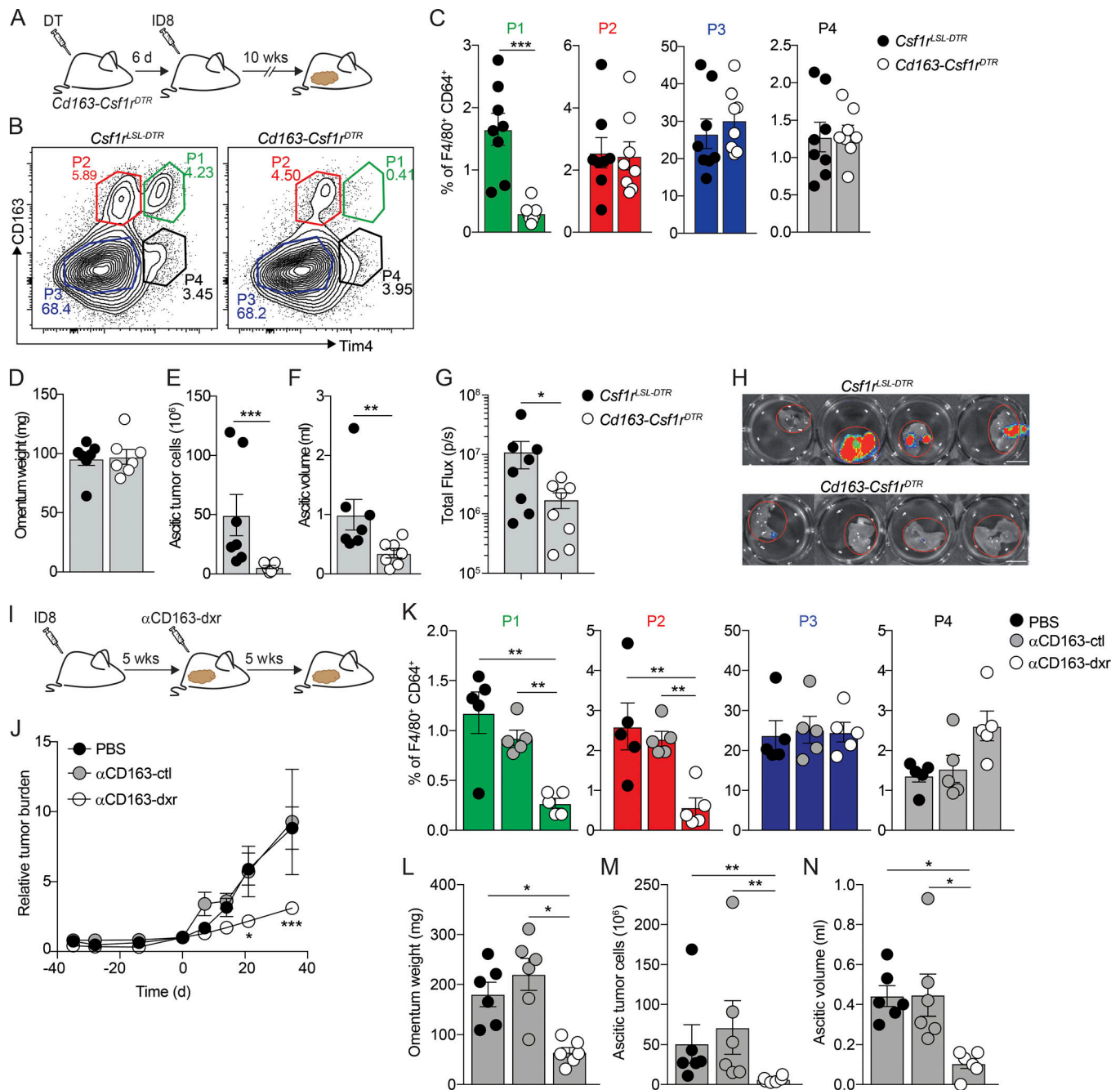


Figure 6. Specific depletion of CD163⁺ Tim4⁺ tissue-resident macrophages prevents metastatic spread of ovarian cancer. (A) Cohorts of *Cd163-Csf1r^{DTR}* or control mice (*Csf1r^{LSL-DTR}*) were injected with 4 ng/kg DT 6 d before transplantation with ID8 cells. Mice were analyzed for depletion of macrophages and effects on tumor growth at 10 wk. (B and C) Flow cytometry analysis of CD163^{hi} Lyve-1⁺ macrophages in omentum of *Cd163-Csf1r^{DTR}* and *Csf1r^{LSL-DTR}* mice 10 wk after injection of ID8 cells. (D–F) Omentum weight (D), total tumor cells in ascites (E), and ascites volume (F) in *Cd163-Csf1r^{DTR}* and *Csf1r^{LSL-DTR}* mice treated with DT. (G and H) Ex vivo bioluminescence analysis of metastases on the diaphragm of *Cd163-Csf1r^{DTR}* and *Csf1r^{LSL-DTR}*; scale bar: 0.5 cm. Data are represented as mean ± SEM of *n* = 7, and statistically significant difference was calculated using Mann-Whitney *U* test; *, *P* < 0.05; **, *P* < 0.01; ***, *P* < 0.001. (I) Therapeutic depletion of CD163⁺ macrophages; mice were injected with ID8 cells and after 5 wk randomized into groups and treated with dxr-loaded αCD163-LNPs (αCD163-dxr), empty αCD163-LNPs (αCD163-ctrl), or PBS alone twice a week for 5 wk. (J) Tumor burden monitored by in vivo bioluminescent imaging. Data are represented as mean ± SEM of *n* = 6, and statistically significant difference was calculated using two-way ANOVA followed by Tukey post hoc test; *, *P* < 0.05; ***, *P* < 0.001. (K) Flow cytometry analysis of P1–P4 macrophages in omentum after therapeutic depletion of CD163⁺ cells. (L–N) Omentum weight (L), total tumor cells in ascites (M), and ascites volume (N). Data are represented as mean ± SEM of *n* = 6, and statistically significant difference was calculated using Kruskal-Wallis one-way ANOVA followed by Dunn’s multiple comparisons test; *, *P* < 0.05; **, *P* < 0.01; ***, *P* < 0.001. All data are representative of three independent experiments.

of invasive disease (Fig. 6). To further explore the phenotype of ascitic ID8 cells and define the mechanisms behind this invasive transition, we performed transcriptomic analysis of cultured ID8 cells and tumor cells isolated from malignant ascites 11 wk after transplantation (ID8-A11). ID8 and ID8-A11 cells were sorted by flow cytometry, and RNAseq libraries were prepared directly from frozen cell pellets. To identify meaningful biological processes that are affected in ID8-A11 cells compared with parental ID8 cells, we performed a GO term-based gene set enrichment analysis (GSEA; Fig. S5 E); GO terms are represented by nodes that are colored according to the normalized enrichment score. GO terms that share DEGs are grouped together, generating clusters, thus indicating common biological processes. With this analysis, we found clusters of GO terms up-regulated in ID8-A11 cells that represent biological processes often associated with metastatic tumor cells, including drug metabolism, epithelial cell migration, organization of cell junctions, and organ development (Fig. S5 E, red). In contrast, clusters of GO terms that were down-regulated in ID8-A11 cells were mainly linked with biological processes associated with cell division such as cytokinesis, cell cycle, DNA repair, and replication (Fig. S5 E, blue). To further explore these pathways, we performed GSEA; in accordance with a metastatic phenotype, GSEA showed a positive enrichment of gene sets associated with EMT and down-regulation of genes associated with cell cycle and cell division (Fig. S5 F). The inverse enrichment of EMT pathways versus cell division, coupled with the up-regulation of WNT, NOTCH, and STAT3 signaling (Fig. S5 F), suggested that ID8-A11 cells may have acquired a CSC-like phenotype. Ascitic tumor cells with CSC characteristics have been associated with advanced human ovarian cancer, where they form multilayered spheroid structures (Bapat et al., 2005). To assess the CSC-like phenotype of ascitic ID8 cells compared with ID8 cells in omentum, we next compiled a list of genes that were reported as biomarkers of ovarian CSCs (Table S1) and analyzed their expression in ascitic ID8 cells (ID8-A11) compared with cells in the omentum (ID8-OM). This analysis confirmed an up-regulation of most CSC markers in ascitic ID8 cells (Fig. 7 A, Cluster III). In addition, we established a panel of cell-surface CSC markers and measured their expression by flow cytometry. In agreement with gene expression analysis, ID8-A11 cells showed increased expression of a number of surface markers for CSCs, including CD44, CD54, CD55, CD106, and CD117, as compared with ID8 cells in omentum (Fig. 7 B). As mentioned above, spheroid formation is a functional characteristic of CSCs, as is the increased activity of aldehyde dehydrogenase (ALDH; Kim et al., 2018). In contrast to cultured ID8 cells, ascitic ID8-A11 cells rapidly formed spheroids in vitro (Fig. 7, C and D). In addition, flow cytometry analysis of ALDH activity using the Aldefluor assay showed increased ALDH activity in ID8-A11 cells (Fig. 7 E). Finally, acquisition of CSC characteristics is associated with increased tumor-initiating potential and metastatic spread. We therefore injected cohorts of mice with either ID8 or ID8-A11 cells and followed tumor burden and spread in vivo using bioluminescence. The overall tumor burden in mice injected with ID8-A11 cells was already significantly increased after 20 d, whereas parental ID8 cells still had not established significant tumors

(Fig. 7 F). Moreover, when tumors did establish in mice injected with ID8 cells, these were restricted to the omentum, whereas ID8-A11 cells had spread throughout the peritoneal cavity (Fig. 7 G). This was further substantiated in ex vivo analysis that showed increased growth of ID8 cells in omentum at this time point and the absence of ascites, whereas ID8-A11 cells showed reduced growth in omentum and generated considerable ascitic tumor growth (Fig. 7, H and I). These studies demonstrated that the transition to invasive disease in this model was associated with the acquisition of CSC characteristics by ascitic tumor cells.

CD163⁺ Tim4⁺ tissue-resident macrophages promote the CSC-like phenotype of ovarian cancer cells

We next evaluated the impact of tissue-resident macrophages in omentum on the acquisition of CSC characteristics by ascitic ID8 cells. CD163⁺ macrophages in the omentum were depleted by three consecutive injections of CD163-targeted cytotoxic LNPs (α CD163-dxr) on days 1, 3, and 5, and control mice were injected with either vehicle or empty LNPs (α CD163-ctrl). Monocyte-derived CD163⁺ macrophages (P2) were then allowed to recover before injection of ID8 cells on day 8, and the development of invasive disease was analyzed at 10 wk (Fig. 8 A). Specific depletion of resident CD163⁺ Tim4⁺ macrophages (P1) in omentum was confirmed by flow cytometry (Fig. 8, B and C), as was the impaired development of invasive disease, including the number of ascitic tumor cells and peritoneal metastases (Fig. 8, D–G). To evaluate the impact on CSC-like phenotype in ID8 cells, we next analyzed the expression of our CSC marker panel by flow cytometry on ascitic ID8 cells from control-treated mice and after depletion of resident omental macrophages (Fig. 7 B and Table S1). We then conducted an unsupervised gating analysis and dimensionality reduction using t-distributed stochastic neighbor embedding (tSNE). Samples corresponding to individual treatment groups were subsequently gated out and replotted as individual tSNE plots (Fig. 8 H). This analysis showed that ascitic tumor cells from α CD163-dxr-treated mice, specifically lacking resident CD163⁺ Tim4⁺ macrophages in the omentum, clearly separated from ascitic tumor cells in control mice (Fig. 8 H, green versus red/blue, respectively). Subsequent color mapping of the staining intensity for each of the CSC markers revealed a loss of tumor cells expressing CD54, CD55, CD106, and CD117 in α CD163-dxr-treated mice (Fig. S5 G). The reduced frequency of CD54-, CD55-, CD106-, and CD117-expressing cells was subsequently confirmed by manual gating. This showed that in control mice >60% of ascitic ID8 cells expressed CSC markers, which was reduced to <20% upon depletion of resident CD163⁺ Tim4⁺ macrophages in the omentum (Fig. 8 I). Thus, the specific depletion of resident omental macrophages resulted in reduced accumulation of ascitic tumor cells with a CSC-like phenotype. The acquisition of CSC characteristics is frequently associated with EMT (Nieto et al., 2016), and our previous transcriptomic analysis of ascitic ID8 cells showed an up-regulation of EMT-associated genes (Fig. S5 F). To confirm these data, we analyzed the expression of transcription factors (TFs) known to drive either EMT or the reverse process known as mesenchymal-to-epithelial transition (MET) in ID8-A11 cells. This analysis confirmed an increased gene expression of TFs

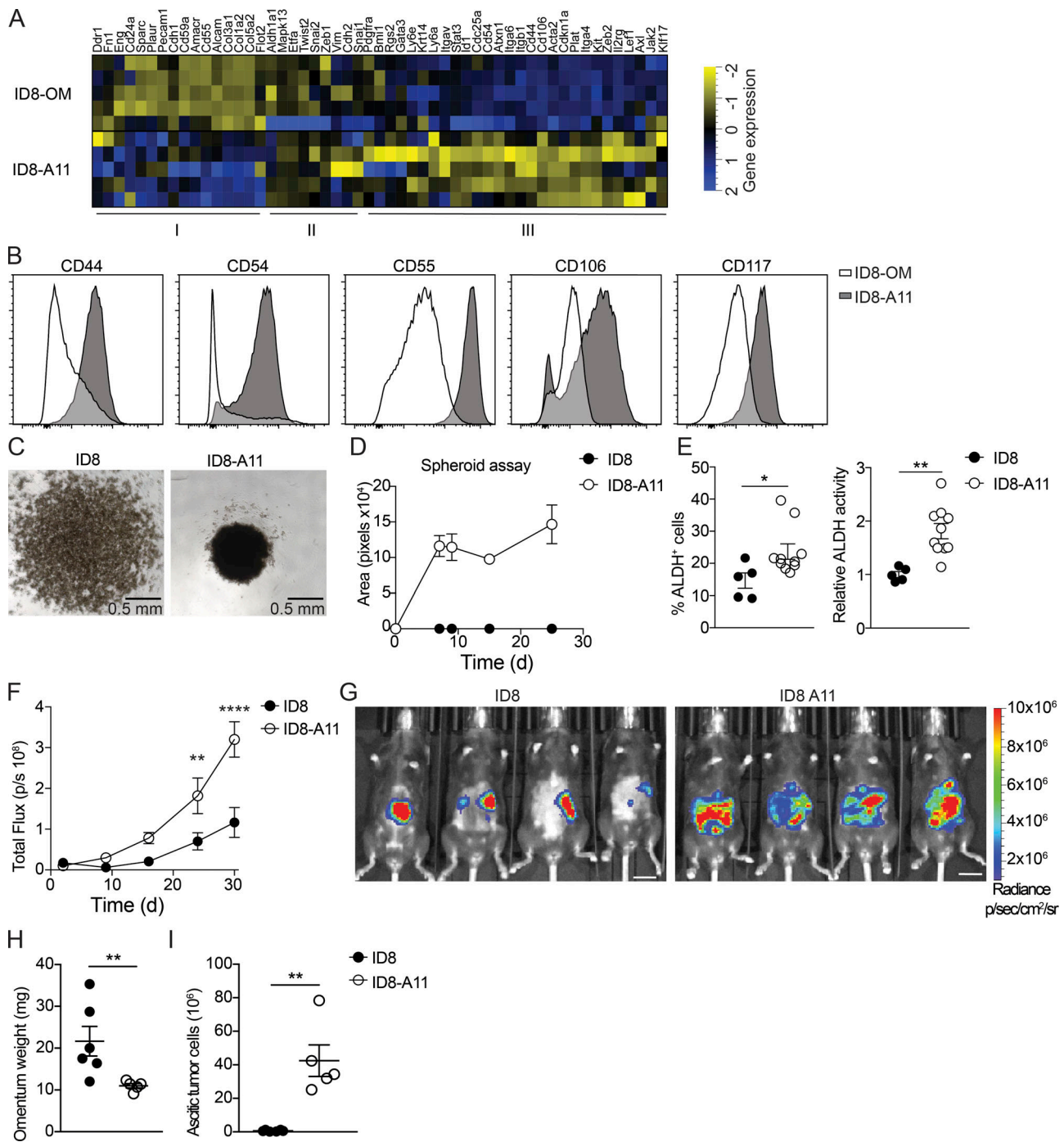


Figure 7. Ovarian cancer cells in ascites acquire CSC characteristics. (A) Heatmap showing expression of CSC markers in omental ID8 cells (ID8-OM) and ID8 cells from ascites (ID8-A11); see Table S1 for details. **(B)** Flow cytometry analysis of CSC surface markers on ascitic ID8-A11 cells compared with ID8 cells in omentum (ID8-OM). **(C and D)** Spheroid formation assay comparing cultured ID8 and ID8-A11 cells; 4×10^4 cells were seeded in ultra-low-adherence 96-well plates, and formation of spheroids was assessed with a wide-field microscope. **(E)** Analysis of ALDH activity in ID8 and ID8-A11 cells by flow cytometry using the Aldefluor assay. ALDH⁺ cells were gated using DEAB-treated cells as negative control (left), and relative ALDH activity was calculated by measuring the median fluorescence intensity of Aldefluor. Data are represented as mean \pm SEM of $n = 5$ (ID8) or $n = 8$ (ID8-A11), and statistically significant difference was calculated using Mann-Whitney *U* test; *, $P < 0.05$; **, $P < 0.01$. **(F)** Analysis of tumorigenic potential of ID8 and ID8-A11 cells in vivo; total tumor burden was monitored by in vivo bioluminescence imaging. Data are represented as mean \pm SEM of $n = 6$, and statistically significant difference was calculated using two-way ANOVA followed by Tukey post hoc test; **, $P < 0.01$; ****, $P < 0.0001$. **(G)** Representative images of tumor localization at 30 d after injection of parental ID8-Luc and ID8-A11 cells; scale bar: 1 cm. **(H and I)** Ex vivo analysis of tumor burden in omentum (H) and ascites (I) at 30 d after transplantation of ID8-Luc or ID8-A11 cells. Data are represented as mean \pm SEM of $n = 6$ (ID8) or $n = 5$ (ID8-A11), and statistically significant difference was calculated using Mann-Whitney *U* test; **, $P < 0.01$. All data are representative of two independent experiments.

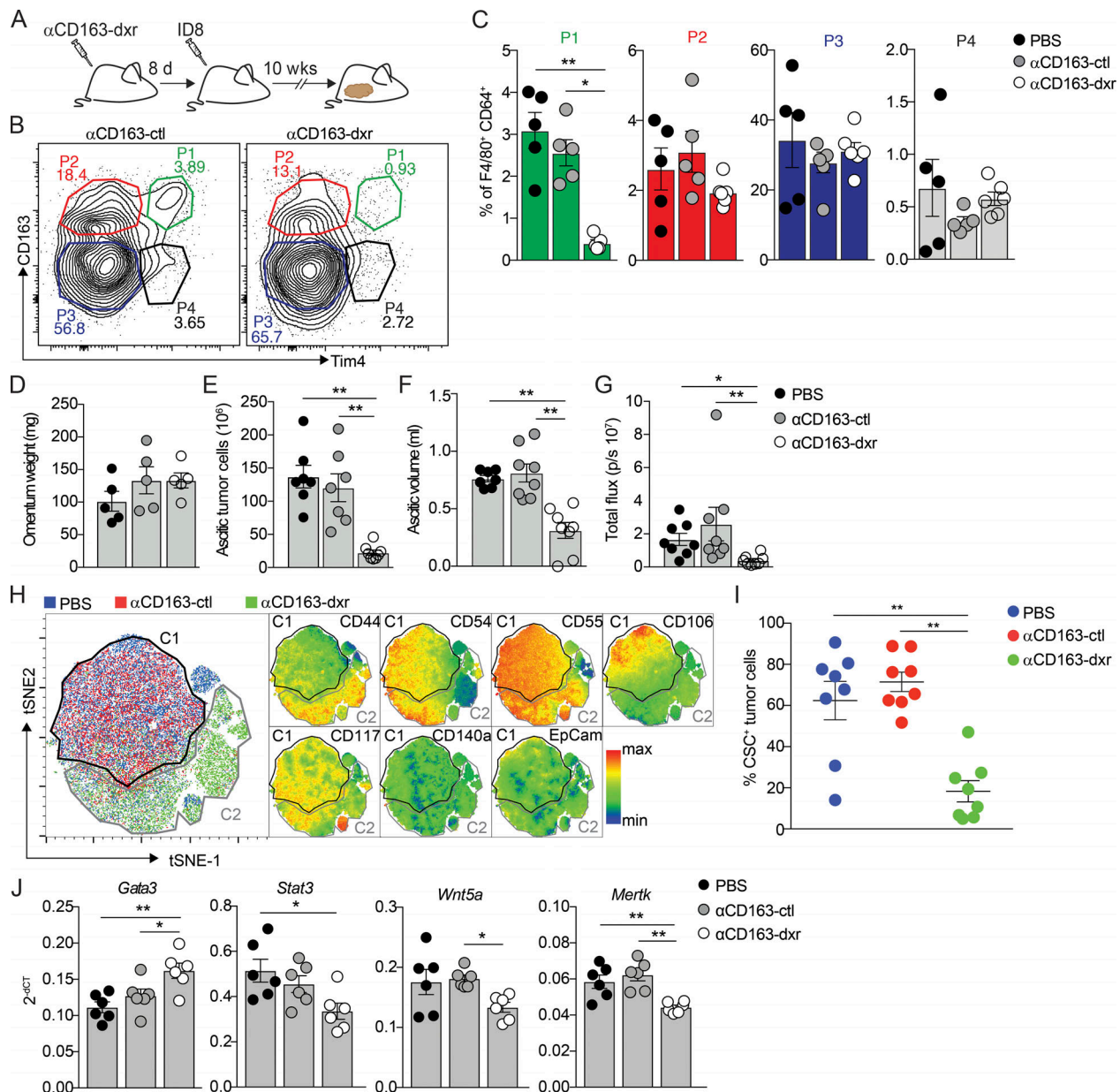


Figure 8. CD163⁺ Tim4⁺ tissue-resident macrophages promote the CSC-like phenotype of ovarian cancer cells. (A) Specific depletion of CD163⁺ Tim4⁺ (P4) macrophages using dxr-loaded αCD163-LNPs (αCD163-dxr); mice were injected i.p. with 1 mg/kg αCD163-dxr or controls (empty αCD163-LNPs or PBS) on days 1, 3, and 5, before injection of ID8-Luc cells on day 8. (B and C) Flow cytometry analysis of CD163^{hi} Lyve-1⁺ macrophages in omentum at 10 wk after prophylactic treatment with αCD163-dxr. Data are represented as mean ± SEM of *n* = 5 (PBS, αCD163-LNP) or *n* = 6 (αCD163-dxr), and statistically significant difference was calculated using Kruskal-Wallis one-way ANOVA followed by Dunn's multiple comparisons test; *, *P* < 0.05; **, *P* < 0.01. (D-F) Omentum weight (D), total tumor cells in ascites (E), and ascites volume (F) at 10 wk after prophylactic treatment with αCD163-dxr. (G) Ex vivo bioluminescence analysis of metastases on the diaphragm. Data are represented as mean ± SEM of *n* = 8, and statistically significant difference was calculated using Kruskal-Wallis one-way ANOVA followed by Dunn's multiple comparisons test; *, *P* < 0.05; **, *P* < 0.01. (H) tSNE map of concatenated fcs files from flow cytometry analysis of tumor cells from ascites after prophylactic treatment with αCD163-dxr. tSNE parameters were computed on expression levels of CSC markers (CD44, CD54, CD55, CD106, CD117, CD140a, and EpCam), and individual sample files were color-coded according to treatment group (PBS, blue; αCD163-LNP, red; αCD163-dxr, green; *n* = 8). This analysis identified distinct clusters from control-treated mice (PBS or αCD163-LNP; C1, black) and αCD163-dxr-treated mice (C2, gray). Expression of the individual CSC markers was subsequently visualized by heatmap statistics in a tSNE map of the concatenated samples within C1 (PBS or αCD163-LNP) and C2 (αCD163-dxr; right). (I) Flow cytometry analysis identifying the proportion of malignant cells expressing specific CSC markers: CD54, CD55, CD106, and CD117. See Fig. S5 G for the gating strategy. Data are represented as mean ± SEM of *n* = 8, and statistically significant difference was calculated using Kruskal-Wallis one-way ANOVA followed by Dunn's multiple comparisons test; **, *P* < 0.01. (J) Gene expression analysis of *Gata3*, *Stat3*, *Wnt5a*, and *Mertk* in tumor cells from omentum after specific depletion of CD163⁺ Tim4⁺ (P1) macrophages, as described in A. dCT, delta cycle threshold. Data are represented as mean ± SEM of *n* = 6, and statistically significant difference was calculated using Kruskal-Wallis one-way ANOVA followed by Dunn's multiple comparisons test; *, *P* < 0.05; **, *P* < 0.01. A-G are representative of three independent experiments, whereas H-J are representative of two independent experiments.

driving EMT (e.g., *Zeb2*), whereas TFs involved in MET were down-regulated (e.g., *Gata3*; Fig. S5 H). Interestingly, *Gata3* alone was recently shown to be sufficient to reverse EMT and inhibit metastases in breast and colon cancer (Yan et al., 2010; Yang et al., 2017). Since EMT has been suggested to precede the acquisition of CSC characteristics, we evaluated the expression of EMT/MET regulators in ID8 cells from omentum after depletion of CD163⁺ Tim4⁺ resident macrophages. Mice were treated as described above, ID8 tumor cells were isolated from the omentum, and expression of EMT- and MET-associated TFs was analyzed. We observed a significant increase in gene expression of *Gata3* in ID8 cells from omentum after depletion of resident macrophages, which was accompanied by decreased expression of *Stat3*, *Wnt5a*, and *Mertk* (Fig. 8 J), all positive regulators of EMT and CSC phenotype.

In summary, these experiments showed that the acquisition of EMT and CSC characteristics by ID8 cells and the development of invasive disease are promoted by the presence of resident CD163⁺ Tim4⁺ macrophages in omentum.

Discussion

The vast majority of cancer-related deaths are due to the development of metastatic disease. The metastatic spread of cancer can be described according to two basic models. The predominant linear model dictates a stepwise progression of primary tumors before dissemination of fully metastatic malignant cells. However, the parallel model accounts for the early dissemination of cancer cells and the formation of distant metastases that develop in parallel with the primary tumor. While there has been extensive research into the stepwise progression of primary tumors toward a metastatic phenotype, relatively little is known about the role of cells that form the premetastatic niche for disseminated cancer cells and their involvement in the metastatic spread of disease. Given that macrophages populate all adult tissues and the proven role of TAMs in promoting invasion and metastasis in experimental models (Noy and Pollard, 2014), it is likely that resident macrophages form an important component of the tissue niche for the malignant progression of disseminated cancer cells.

It had previously been assumed that TAMs are mainly monocyte derived (Lahmar et al., 2016; Yang et al., 2018), until several recent studies showed that macrophages of embryonic origin can persist in tumors from experimental models and may have distinct contributions toward tumor progression (Zhu et al., 2017; Loyher et al., 2018). However, these studies were limited by the lack of specific markers to distinguish TAM subsets on the basis of their origins and tools to specifically target these subsets. For example, Zhu et al. (2017) used parabiosis and fluorescent fate-mapping tools in a model of pancreatic ductal adenocarcinoma to identify a population of MHCII^{lo} TAMs of embryonic origin that were maintained independently of blood monocytes. However, to assess the contribution of these cells to tumor growth, the authors used an aggressive pan-targeting strategy combining both clodronate liposomes and CSF1 blockade to efficiently deplete all tissue-resident macrophages.

Here, we studied the origins and function of macrophage subsets in a model of metastatic ovarian cancer, using a novel intersectional transgenic approach and antibody-targeted cytotoxic liposomes to specifically deplete CD163⁺ macrophages. We describe how tissue-resident CD163⁺ macrophages in omentum play a specific role in the malignant progression of ovarian cancer and the development of invasive disease. We showed that ovarian cancer cells injected into the peritoneal cavity infiltrate the omentum in the vicinity of FALCs and in close contact with resident CD163⁺ macrophages. Using single cell transcriptomics, flow cytometry, and whole-mount imaging, we identified distinct subsets of CD169⁺ Lyve-1⁺ mature macrophages in omentum based on their expression of CD163 and Tim4. CD163 has been used extensively as a marker of tissue macrophages in humans, where the frequency of CD163⁺ TAMs shows a striking correlation with poor clinical outcome in a range of cancers (Komohara et al., 2014). Conversely, few studies have addressed the expression of Tim4 in human macrophages. Recent studies have shown that Tim4 is expressed by a range of long-lived tissue-resident macrophages in mice, including Kupffer cells (Scott et al., 2016), large peritoneal macrophages (Rosas et al., 2014), and gut and cardiac macrophages (Dick et al., 2019; De Schepper et al., 2018), and is thus emerging as a marker of tissue-resident macrophages with potential for self-renewal. When analyzing the ontogeny of CD169⁺ Lyve-1⁺ macrophages in omentum, we found that Tim4 expression alone did not distinguish long-lived cells, since Tim4⁺ CD163⁻ macrophages (P4) were monocyte derived and rapidly replaced by bone marrow-derived cells. However, CD163⁺ Tim4⁺ (P1) macrophages were uniquely independent of bone marrow-derived monocytes in the adult, in both steady state and during tumor development, and at least a proportion of these cells were shown to be of embryonic origin. In contrast, CD163⁺ Tim4⁻ macrophages (P2) were relatively long lived at steady state, compared with CD163-negative cells, but were quickly replaced by monocyte-derived cells after tumor initiation. Transcriptomic analysis revealed a close relationship between CD163⁺ P1 and P2 macrophages at steady state, but during tumor development, monocyte-derived Tim4-negative P2 macrophages significantly diverged from Tim4⁺ P1 cells and became more similar to short-lived CD163-negative monocyte-derived cells (P3). In fact, the phenotype of CD163⁺ Tim4⁺ resident macrophages in omentum was remarkably stable during tumor progression, suggesting that these cells maintain a level of tissue imprinting that is lost from more short-lived cells. Transcriptomic analysis of these different TAM subsets suggested functional diversification during tumor growth. Resident CD163⁺ Tim4⁺ (P1) macrophages showed a unique enrichment of pathways regulating JAK-STAT signaling, also previously linked with macrophage self-renewal (Soucie et al., 2016). However, other pathways previously associated with tumor-promoting functions, such as angiogenesis, blood vessel development, and tissue remodeling, were shared between both monocyte-derived and resident CD163⁺ populations (P1 and P2).

Prophylactic depletion of CD163⁺ macrophages, allowing recovery of monocyte-derived CD163⁺ Tim4⁻ cells, revealed an important and specific role for resident CD163⁺ Tim4⁺ omental

macrophages in the development of invasive disease. However, therapeutic depletion of both P1 and P2 CD163⁺ TAMs using cytotoxic liposomes had a major impact on both primary tumor growth and invasive disease, suggesting that monocyte-derived and tissue-resident CD163⁺ TAMs have distinct roles in disease progression. We recently showed that depletion of monocyte-derived CD163⁺ TAMs in a mouse melanoma model led to a T cell-mediated regression of tumor growth (Etzerodt et al., 2019), which may also account for the observed reduction in omental tumor burden upon depletion of monocyte-derived CD163⁺ macrophages in this model.

Macrophages play important roles in organogenesis and tissue remodeling (Pollard, 2009) and have been shown to affect epithelial cell plasticity and stimulate tissue stem cells (Chakrabarti et al., 2018; Lee et al., 2018). The acquisition of stem-like characteristics by cancer cells (CSCs) has been suggested to promote tumor progression and metastasis (Kreso and Dick, 2014). CSCs show increased anchorage-independent survival and high levels of resistance to chemotherapy or radiotherapy and thus have major implications for disease recurrence from disseminated tumor cells. EMT is also frequently associated with CSCs and accounts for the acquisition of migratory and invasive properties (Nieto et al., 2016). Several reports have shown that ascitic tumor cells from late-stage ovarian cancer patients show CSC-like characteristics (Lupia and Cavallaro, 2017; Bapat et al., 2005), which may explain the rapid progression of late-stage disease in these patients and the high frequency of disease recurrence. When analyzing the transcriptome of ascitic tumor cells in our model, we found a significant enrichment of pathways associated with CSCs and EMT. Interestingly, not only did the specific depletion of CD163⁺ Tim4⁺ resident macrophages in omentum decrease the formation of malignant ascites, it also reduced the frequency of CSCs among the few ascitic tumor cells that did accumulate. Analysis of tumor cells in the omentum showed that genes associated with regulation of EMT and CSCs, namely Stat3 (Abubaker et al., 2014), Wnt5a (Ford et al., 2014), and Mertk (Jung et al., 2016), were down-regulated in tumor cells when CD163⁺ Tim4⁺ macrophages were absent, whereas Gata3, a negative regulator of EMT, was up-regulated. In this regard, it is of particular interest that clustering analysis showed that CD163⁺ Tim4⁺ macrophages were enriched for genes associated with positive regulation of the JAK-STAT pathway. This included IL6, EPO, and prolactin, all of which activate STAT3 and have previously been shown to promote EMT and the acquisition of CSC characteristics in ovarian cancer (Solar et al., 2008; Wang et al., 2018; Levina et al., 2009). Future studies will elucidate the molecular basis of the dialog between tissue-resident macrophages and ovarian cancer cells leading to the up-regulation of JAK-STAT signaling. Given the conserved role of these pathways in EMT and CSCs, these axes of interaction could be relevant to other cancers associated with the dissemination of premalignant or dormant cancer cells. Of note, tissue-resident macrophages of embryonic origin also dominate the adult mammary gland in the mouse (Jäppinen et al., 2019), and recent studies have shown an important role for mammary gland macrophages in regulating the phenotype of basal stem cells (Chakrabarti et al., 2018).

In summary, our data show that tissue-resident macrophages in omentum play a specific role in the malignant progression of disseminated tumor cells and the development of invasive disease in a mouse model of metastatic ovarian cancer. These studies add significantly to our understanding of TAM heterogeneity and the specific contribution of different macrophage subsets to disease progression. The axes of interaction between tissue-resident macrophages and cancer cells could represent important new therapeutic targets, not only in ovarian cancer but also other cancers where the development of CSCs can have a disastrous impact on disease prognosis.

Materials and methods

Mouse breeding, omentectomy, and ovarian cancer model

Tg(Csf1r-LSL-HBEGFmCherry; Schreiber et al., 2013), Rosa26^{LSL-YFP}, Cx3Cr1^{CreER}, and Cx3Cr1^{GFP/+} were obtained from the Jackson Laboratory. C57BL/6J mice were obtained from Janvier Labs. Ccr2^{-/-} mice and Rosa26^{LSL-tdRFP} mice were gifts from Bernard Malissen (Centre d'Immunologie de Marseille-Luminy [CIML], Marseille, France). Cd163^{iCre} mice were generated from modified embryonic stem cells on a C57BL/6 background as described (Etzerodt et al., 2019). In brief, a FlpO-NeoR cassette encoding IRES-iCre was inserted in the 3'UTR of the CD163 gene using homologous recombination and used to generate chimeric mice that were subsequently crossed to Flp deleter mice to facilitate removal of NeoR cassette. Omentectomy and sham surgery were performed on mice under general anesthesia using 87.5 mg/kg ketamine and 12.5 mg/kg xylazine injected i.p. Laparotomy was performed through a 1-cm incision in the region of the stomach, and omentum was carefully removed. The abdominal wall was then closed in two layers with surgical suture. Sham surgery was performed as described above with the omentum carefully lifted before being placed back in the abdominal cavity. To mimic peritoneal spread of epithelial ovarian cancer, 10⁶ ID8-Luc cells were injected i.p. in 500 μ l of sterile PBS (pH 7.4). Tumor burden was estimated weekly by injecting mice i.p. with 100 mg/kg d-luciferin followed by in vivo bioluminescence imaging using an IVIS Spectrum imager (PerkinElmer). For visualizing infiltration of ID8-cells in omentum, ID8 cells were prelabeled with a Qtracker 705 cell labeling kit (Thermo Fisher Scientific) before i.p. injections in accordance with the manufacturer's instructions. For therapeutic treatment with LNPs, mice were injected with 100 μ l of LNPs (1 mg/kg dxr) by retroorbital injection starting from 5 wk after i.p. injection of 10⁶ ID8-Luc cells. For prophylactic treatment with LNPs or DT, mice were injected i.p. with either 200 μ l of LNPs (1 mg/kg dxr) or 200 μ l of DT (4 ng/kg) starting from 6 d before inoculation of tumor cells. All mice were euthanized at the indicated times, and peritoneal lavages and tissues were collected for cytometric analysis or imaging analysis. Briefly, 3 ml of ice-cold PBS with 2 mM EDTA, pH 8.0 was injected i.p., and after a careful massage to detach all the cells in the cavity, peritoneal fluid was collected through a 23G syringe. Tubes were weighed to determine the recovered lavage volume, and the cell density was assessed using a hemocytometer. All mice were housed at the

Table 1. Antibodies used for flow cytometry analysis

Antigen	Clone	Dye	Catalog number	Supplier
CD45.2	104	BUV737	564880	BD Biosciences
MHCII	M5/114.15.2	A700	56-5321-82	eBioscience
CD11b	M1/70	BV395	563553	BD Biosciences
F4/80	BM8	BV785	123141	Biolegend
CD163	R34	CF405		
CD64	X54-5/7.1	BV711	139311	Biolegend
CD169	SER-4	eFluor660	50-5755-82	Invitrogen
CCR2	475301	APC	FAB5538A	R&D Systems
Ly6C	AL-21	FITC	553104	BD Biosciences
Tim4	54(RMT4-54)	PerCP-Cy5.5	46-5866-82	eBioscience
Siglec F	ES22-10D8	PE	130-102-274	Miltenyi Biotec
CD5	53-7.3	BV605	563194	BD Biosciences
CD19	1D3	BUV661	565076	BD Biosciences
Lyve1	ALY7	A488	53-0443-82	eBioscience
NK1.1	PK136	APC-Cy7	108724	Biolegend
Ly6G	1A8	APC-Cy7	560600	BD Biosciences

animal facility at CIML with water and food provided ad libitum and a 12-h night/daylight cycle. All animal experiments were approved and performed in accordance with the limiting principles for using animals in testing (the three R's: replacement, reduction, and refinement) and approved by the French Ministry of Higher Education and Research.

Fate-mapping experiments

Genetic fate-mapping using Cx3Cr1^{CreER}:R26-YFP mice was performed as previously described (Mossadegh-Keller et al., 2017); pregnant females were pulse-labeled at E16.5 by i.p. injection of 0.1 mg/kg tamoxifen and 0.05 mg/kg progesterone. For fate-mapping in adult tumor-bearing mice, Cx3Cr1^{CreER}:R26-tdRFP mice were injected with 10⁶ ID8-Luc cells i.p. and after 6 wk pulse-labeled with a single dose of 2 mg tamoxifen dissolved in 200 μ l of corn oil by oral gavage. Generation of shielded chimeras was performed as previously described (Goossens et al., 2019); CD45.1 congenic mice were anesthetized with ketamine (150 mg/kg) and xylazine (10 mg/kg) and placed in 6-mm-thick lead cylinders, exposing only the hind legs. With the abdominal area protected, mice were irradiated with 9 Gy and reconstituted with 10⁷ bone marrow cells from CD45.1/2 mice. After 5 wk, chimerism of blood leukocytes was assessed by flow cytometry.

Flow cytometry and cell sorting

Single-cell suspensions were prepared from omentum by digesting the tissue in RPMI 1640 medium with 1 mg/ml collagenase II (Sigma Aldrich), 50 μ g/ml DNaseI (Roche), and 0.1% (wt/vol) BSA for 30 min at 37°C with gentle agitation. Cell suspensions were subsequently passed through a 70- μ m cell strainer (BD Biosciences) and collected by centrifugation. Blood and ascitic cells harvested by peritoneal lavage were used

without further processing. For RBC lysis, cell suspensions were incubated with 0.85% NH₄Cl for 2 min at room temperature, collected by centrifugation, and resuspended directly in FACS buffer (1 \times PBS pH 7.4, 1 mM EDTA pH 8.0, 3% FCS, and 0.1% NaN₃). For flow cytometry, single-cell suspensions were incubated at 4°C for 10 min with 2.4G2 antibody for Fc receptor blocking followed by incubation with the specified antibodies (see Table 1 for details) for 30 min at 4°C. Prior to analysis, cells were incubated with Sytox Blue (Thermo Fisher Scientific) to discriminate dead cells and filtered through a 70- μ m cell strainer. ALDH activity in tumor cells was measured using the Aldefluor kit (Stem Cell Technologies), in accordance with the manufacturer's instructions. In brief, 2 \times 10⁶ cells were incubated with 5 μ l of Aldefluor stock solution or 5 μ l of Aldefluor stock solution in combination with 5 μ l of the ALDH inhibitor diethylaminobenzaldehyde and incubated for 30 min at 37°C. ALDH activity was subsequently measured by flow cytometry relative to DEAB-treated control cells. All flow cytometry analysis was performed with either BD FACS LSR-2 or Fortessa X-20 flow cytometers, whereas cell sorting was performed with BD FACS Aria SORP. All cytometers were equipped with a 350-nm laser (BD Biosciences). Subsequent data analysis was performed using FlowJo software V10.4 for Mac (Tree Star).

Liposome preparation

Long-circulating liposomes encapsulating ddx were prepared and modified for CD163 targeting as previously described (Fritze et al., 2006; Etzerodt et al., 2012). Briefly, liposome formulations were formed using the ethanol-injection method from a mixture of hydrogenated soy L- α -phosphatidylcholine, mPEG2000-PE, and cholesterol (molar ratio of 55:40:5; Lipoid GmbH and Sigma Aldrich). Lipids were dissolved in ethanol at 65°C for 15 min followed by hydration (to 10% EtOH) for 1 h at 65°C in aqueous

buffer suitable for further downstream applications. Liposomes were sized by extrusion 25 times through a 0.1- μ m filter using the Avanti mini-extruder kit (Avanti Polar Lipids) and dialyzed twice against 150 mM NaCl (0.9% NaCl) with a second dialysis being done overnight at 4°C. For remote loading of dxr, lipid was hydrated in 300 mM (NH₄)₂HPO₃. Following extrusion and dialysis, (NH₄)₂HPO₃-containing liposomes were mixed with dxr-HCl for 30 min at 65°C at a dxr:lipid ratio of 1:5. Lipid content, drug content, and encapsulation efficiency were subsequently estimated from high-pressure size-exclusion chromatography (UV absorbance at 210 nm) using a Dionex Ultimate 3000 HPLC system (Thermo Fisher Scientific) equipped with an Ascentis C18 column (Sigma Aldrich). Liposome size was estimated using dynamic light scattering and the DynaPro NanoStar system (Wyatt Technology Europe GmbH). Modification of liposomes for CD163 targeting was done as described previously using the post-insertion method of the α CD163 antibody, clone 3E10B10 (Etzerodt et al., 2012; Torchilin et al., 2001).

Immunohistochemistry and whole-mount immunofluorescence imaging

Omentum was fixed in 1% formalin and either embedded in optimal cutting temperature compound for cryostat sectioning or used directly for whole-mount imaging. For histological analysis, 10- μ m cryostat sections were mounted on glass slides and stained with H&E and visualized on an upright microscope equipped with a 10 \times objective. For whole-mount imaging, omental tissue was incubated with anti-CD163-ATTO565 (Etzerodt et al., 2013), anti-CD169-eFluor660 (Clone Ser4; eBioscience), anti-CD45.2-Alexa488 (Clone 104; Biolegend), and Tim4-Alexa647 (RMT54-4; Biolegend) in 0.1 M Tris pH 7.2, 1% Triton X-100, 0.5% BSA overnight at 4°C. Nuclei were visualized with Hoechst 33342 (Sigma Aldrich). Tissue was subsequently mounted in RapiClear 1.47 for tissue clearing on glass slides with a 0.2-mm iSpacer (SunJin Lab Co.). Images were acquired on a Zeiss LSM780 confocal microscope (Carl Zeiss Microscopy GmbH) using spectral unmixing with a 10 \times or 20 \times objective.

Spheroid formation assay

Tumor cells in ascites were enriched by depleting leukocytes in peritoneal lavage using the CD45.2 magnisort kit (eBioscience) and seeded at 40,000 cells per well in ultra-low-attachment 96-well plates (Corning Life Science) in DMEM supplemented with 4% heat-inactivated FCS. Formation of spheroids was subsequently monitored by microscopy using an inverted microscope equipped with a 4 \times objective.

scRNA-seq

Single-cell tumor suspensions were prepared from mouse omentum infiltrated with epithelial cancer cells 10 wk after inoculation. Macrophages were isolated by flow-assisted cell-sorting gating on CD11b⁺, Lin^{neg}, F4/80⁺, and CD64⁺. Single-cell transcriptomes were generated from roughly 4,000 cells per mouse ($n = 4$; total of 16,510 cells after Cell Ranger filtering) using Chromium Next GEM Single Cell 3' GEM kit v2 and sequenced to a depth of, on average, 45,000 reads per cell using a NovaSeq S2 flow cell. This averaged to \sim 1,400 genes per cell. After

sequencing, samples were processed with 10 \times Genomics Cell Ranger pipeline (version 2.1.0) using mm10 (v2.1.0) reference genome. Filtered read count matrices were analyzed with Seurat (v3.1.0) running in R (v3.6.1). Briefly, samples were normalized with SCTransform (Hafemeister and Satija, 2019; 13,886 genes retained) and subsequently filtered to remove cells with high mitochondrial read contamination (>15%), low gene detection rate indicative of low-quality cells (<200), and high gene detection rate (>4,000) or high read count (>20,000) indicative of doublets. After filtering, 16,392 cells remained. Subsequently, cells were clustered into 10 clusters using Louvain clustering (resolution = 0.5), and UMAP was used to visualize clusters (assay = "SCT," reduction = "pca," dims = 1:10). Cluster marks were identified by comparing each cluster to all other clusters using the default Wilcoxon Rank Sum test and the default logFC threshold (>0.25). Only genes expressed in \geq 25% of cells in either the cluster or all other clusters combined were considered, and only genes up-regulated in the cluster compared with all other clusters combined were reported. The top 10 cluster markers were selected by first sorting by lowest P value and subsequently by highest fold-change. Datasets are available at the European Bioinformatics Institute under accession no. E-MTAB-8593.

Bulk RNAseq and bioinformatics analysis

Library preparation and RNAseq was performed by the GenomEast platform at Institut de Génétique et Biologie Moléculaire et Cellulaire, Strasbourg, France. Full-length cDNA was generated using a Clontech SMART-Seq v4 Ultra Low Input RNA kit (Takara Bio Europe) according to the manufacturer's instructions from 500 cells isolated by cell sorting in PBS buffer containing RNase inhibitor. cDNA was amplified with 14 cycles of PCR for cDNA amplification by Seq-Amp polymerase. 600 pg of preamplified cDNA was then used as input for Tn5 transposon tagmentation by the Nextera XT DNA Library Preparation Kit (96 samples; Illumina) followed by 12 cycles of library amplification. Following purification with Agencourt AMPure XP beads (Beckman-Coulter), the size and concentration of library DNA were assessed on an Agilent 2100 Bioanalyzer. Libraries were sequenced on an Illumina HiSeq4000 platform generating 50-bp reads. Samples were trimmed to remove TruSeq adapters using BBduk (Bushnell, 2014) and subsequently mapped to the mouse genome assembly version mm10 using STAR version 2.5.3a (Dobin et al., 2013) with junction annotation from Ensembl version 79 (Yates et al., 2016). Gene counts obtained directly from STAR were used in gene expression analysis with DESeq2 (Love et al., 2014) using cqn (Hansen et al., 2012) derived normalization factors. SOM clustering analysis was performed using the "kohonen" R package (Wehrens and Kruisselbrink, 2018; Wehrens and Buydens, 2007), while comparative GO analysis was performed using clusterProfiler (Yu et al., 2012). Heatmaps and hierarchical clustering were generated using the One minus Pearson correlation, and PCA plots with network analysis (using Pearson correlation) to show the three nearest neighbors were generated using Qlucore Omics Explorer (Qlucore AB). Datasets are available at the European Bioinformatics Institute under accession no. E-MTAB-8140 and E-MTAB-8141.

Table 2. **Primer sequences used in gene expression analysis**

Gene	Forward primer 5' to 3'	Reverse primer 5' to 3'
Acta2	CCTCATGCCATCATGCGTCT	AATCTCACGCTCGGCAGTAG
Alcam	GAGGCAGACGATATAAGTGATGAAA	AGACCAACGACAATCCCACA
Aldh1a1	GATGCCGACTTGACATTGC	ATGCTGCGACACAACATTGG
Amacr	CGAGAATTTCTGGCCCGAGG	AGTTTCTCCATGACACCGCAG
Atxn1	CAGAGCATAGTGAATGCTAATCCG	GGCCCTTCATGGGAATCAT
Axl	CTCCACGTGGTTCCAGACA	AGATACCCACCCCATCGTCT
Bmi1	TCAGAGCAGATTGGATCGGAA	GCTGTGGGCATCGTAAGTA
Cd106	GTGGTAAGGAATGAGGGGGC	CTTCAGGGATGAGTAGACCTCC
Cd24a	ACCCACGCAGATTTACTGCAA	AGCGTTACTTGGATTGGGGA
Cd44	TTCCTTCGATGGACCGGTTA	TACTCGCCCTTCTTGCTGTA
Cd54	GGACCACGGAGCCAATTTCT	TAGCTGGAAGATCGAAAGTCCG
Cd55	AACACAGGTGGTGACCATTAT	TTTCTTCGTAACCTTTCGTTGGC
CD59a	TATGCTGTAGCCGGAATGCAA	CCCCAAGGATCCGTCACTTTT
Cdc25a	GCAAACCTTGCCGATCGTTG	TCTGCTCTCTTCAACACCGC
Cdh1	TCGCCACAGATGATGGTTCA	TTCGAGGTTCTGGGATGGGA
Cdh2	AAAGCCTGGGACGTATGTGA	ATGTTGGGTGAAGGTGTGCT
Cdkn1a	ATCCAGACATTAGAGCCACAG	AGACAACGGCACACTTTGCT
Col3a1	ACGTAAGCACTGGTGGACAG	GAGGGCCATAGCTGAAGTAA
Col5a2	AAGGCTGGTGATCAAGGTGT	CCCCAGGCAGTCCAGTTATC
ddr1	ATCGGTTGCGTTACTCCCG	CGTTACCCGAAATCACCTCC
Eng	CTGCGGCATGAAAGTGACAG	ACTTTTTCCGAAGTGGTGGT
Etfa	TCAGAGTGGCTTGACCAGAA	CTCTTCAAACCCCGACCACC
Fn1	ATACCGTTGTCCAGAGGTG	GGAAGAGTTTAGCGGGGTCC
Gata3	GCTACTCAGTGATCGGAAGA	GAGAGGAATCCGAGTGTGACC
Flot2	TGGTCTCAGGAGGCTGTTGT	GTGTCCGAGATACACCACCA
Id1	GAGTCTGAAGTCGGGACCAC	GAACACATGCCGCTCG
Il2rg	TGAGCCTCAGGCAACCA	AGTGACTGCACTCCTGGAA
Itga4	GCACTCTACAACCTGGACC	GATGAGCCAGCGCTTCGAC
Itga6	GTTTTTACTGTGGAAGTGTGGCT	CCTTGTGATAGTGGCATCGT
Itgav	AGGAGATCGCCACCTACCG	GAGGTACATCTCTGGATGACTGA
Itgb1	GGTCAGCAACGCATATCTGG	GCCAAATCAGCGATCCACAAA
Jak2	AAAGCTTGTGGTATTACGCTCG	TGGAAGACATGATTGGGTGGG
Kit	CCATAGACTCCAGCGTCTTCC	TGGGCTGGATTTGCTCTTTA
Klf17	CACCAGCCTCCATGGATAAT	TGGCTGGTGGCTGATGAAAT
Krt14	AGGAGATCGCCACCTACCG	GAGGTACATCTCTGGATGACTGA
Lef1	CATCACGGGTGGATTCAGGC	GATGGGAAAACCTGGACATGGA
Ly6a	CTGTGTGCAGAAAGAGCTCAGG	GAATCCACAATAACTGCTGCCTC
Ly6e	TTATCTTCGGGGCCTCTTAC	TCAGGAATGAACCTGCTCCAT
Mapk12	CGTGGACGAATGGAAACAACA	GTGAGTCCTTCCGGGCTATG
Pdgfra	ACCTCAGAGAGAATCGGCC	CCATAGCTCCTGAGACCCGC
Pecam1	GAGAGTGACAGCGGGGAGTA	AGAGCATTTCGCACACCTGG
Plat	CCTGACCAGGGAATACATGGG	TTGTCTGCGTTGGCTCATCT
Plaur	TTGGGTGTTCTCCGAAGAG	TTTCCAGCACATCTAAGCCT
Rgs2	AGTAAATATGGGCTGGCTGCAT	TTGAGGACAGTTTTTGGGGTGA

Table 2. Primer sequences used in gene expression analysis (Continued)

Gene	Forward primer 5' to 3'	Reverse primer 5' to 3'
Snai1	TAGGTCGCTCTGGCCAACAT	CTGGAAGGTGAACCTCCACACA
Snai2	ACATTAGAACTCACACTGGGGAA	GCCCTCAGGTTTGTCTGTCT
Sparc	GGAACATTGCACCACACGTT	TCCTTGTTGATGTCCTGCTCC
Stat3	TTCCCAAGGAGGAGGCATTTG	GACATCGGCAGGTCAATGGTAT
Twist2	CTCACGAGCGTCTCAGCTAC	AGATGTGCAGGTGGGTCCTG
Vim	GCGAGAGAAATTGCAGGAGGA	CGTTCAAGGTCAAGACGTGC
Zeb1	ACACAAGCGAGAGGATCATGG	ATAATTTGTAACGTTATTGCGCCG
Zeb2	TTCGCGGCTTCTTCATGCTT	GGCTCGATCTGTGAAGTCTTGTT
Mertk	CAAAGTAATCCCTCCCCGC	AGTTCCTTGACCTGAATGCT
Wnt5a	TTTGGATTGTCCCCAAGGC	ATTCCAATGGGCTTCTTCATGG
Ppia	ATGGTCAACCCACCCTG	TTCTTGCTGTCTTTGGAACTTTGTC

Gene expression analysis

Total RNA was purified from sorted cell populations using the RNeasy Micro Kit (Qiagen), and concentration was determined using the Quant-IT RiboGreen RNA assay kit (Thermo Fisher Scientific). First-strand cDNA synthesis was performed with a High Capacity cDNA Reverse Transcription Kit (Thermo Fisher Scientific) followed by preamplification of genes of interest using the Fluidigm PreAmp Master Mix (Fluidigm Europe B.V.) with 25 ng of total RNA and in accordance with the manufacturer's instructions. Exon-spanning primers to amplify genes of interest were designed using Primer-Blast (see Table 2 for details). To increase sensitivity, genes of interest were pre-amplified by 12 cycles of PCR using pooled assays followed by exonuclease I treatment (New England Biolabs) to remove unincorporated primers. Final preamplified cDNA was diluted 1:5 in Tris-EDTA buffer. Gene expression analysis was performed using the Biomark HD system from Fluidigm (Fluidigm Europe B.V.) in accordance with the manufacturer's instructions and standard settings. Data were analyzed using the Real-Time PCR Analysis Software (Fluidigm Europe B.V.), and the resulting cycle threshold values were normalized to *Ppia* to obtain delta CT values.

Statistical analysis

For treatment studies, statistical analysis was performed using two-way ANOVA followed by Tukey post-hoc test. For comparison between groups, statistical testing was performed using nonparametric tests such as Mann-Whitney *U* test or Kruskal-Wallis followed by Dunn's multiple comparisons test. *P* values are indicated as *, *P* < 0.05; **, *P* < 0.01; ***, *P* < 0.001; and ****, *P* < 0.0001. All statistical analysis was performed with Graphpad Prism 7 for Mac.

Online supplemental material

Fig. S1 shows the gating strategy for macrophages in omentum. Fig. S2 shows the flow cytometric analysis of monocytic chimerism in the shielded chimera fate-mapping experiments. Fig. S3 shows a heatmap of the 5,000 most DEGs in CD169^{hi} Lyve-1⁺ omental macrophages sorted at steady state (0 wk) or 5 wk and 10 wk after infiltration of ID8 ovarian cancer cells. Fig. S4 shows

tumor growth in *Ccr2*^{-/-} mice as well as replenishment of omental and peritoneal macrophages after prophylactic depletion of CD163⁺ macrophages in *Cd163-Csf1r*^{DTR} mice. Fig. S5 shows heatmaps of genes associated with enriched pathways in P1-P3 omental macrophages. Fig. S5 also shows the transcriptomic comparison of cultured ID8 cells with ID8 cells harvested from ascites. Table S1 lists markers associated with CSC phenotype in ovarian cancer.

Acknowledgments

We thank Bernard Malissen (CIML, Marseille, France) for Rosa26-LSL-tdRFP and *Ccr2*^{-/-} mice, Lionel Chasson (histology platform, CIML) for assistance with histology, and Sylvain Bigot (flow cytometry platform, CIML) for help with cell sorting. scRNAseq was carried out at the Center for Functional Genomics and Tissue Plasticity, Functional Genomics & Metabolism Research Unit, University of Southern Denmark. The authors thank Tenna P. Mortensen and Ronni Nielsen for sequencing assistance.

These studies were supported by grants to A. Etzerodt from the Novo Nordisk Foundation (NNF14OC0008781) and to T. Lawrence from the Agence Nationale de la Recherche (ANR-09-MIEN-029-01 and ANR-10-BLAN-1302-01), FP7 Ideas: European Research Council 2007-2013 grant agreement number 260753, and institutional funding from Institut national de la santé et de la recherche médicale, Centre national de la recherche scientifique, and Aix Marseille Université. Microscopy facilities are supported by France Bio Imaging grant ANR-10-INBS-04-01.

Author contributions: A. Etzerodt and T. Lawrence designed the experiments. A. Etzerodt and M. Moulin performed the experiments with help from M. Delfini, M. Bajenoff, N. Mossadegh-Keller, M.H. Sieweke, S.K. Moestrup, and N. Auphan-Anezin. T.K. Doktor performed bioinformatic analysis. A. Etzerodt and T. Lawrence wrote the manuscript with comments from S.K. Moestrup, M.H. Sieweke, and N. Auphan-Anezin.

Disclosures: Dr. Etzerodt reported personal fees from Stipe Therapeutics outside the submitted work. No other disclosures were reported.

Submitted: 3 October 2019
 Revised: 23 November 2019
 Accepted: 16 December 2019

References

- Abubaker, K., R.B. Luwor, H. Zhu, O. McNally, M.A. Quinn, C.J. Burns, E.W. Thompson, J.K. Findlay, and N. Ahmed. 2014. Inhibition of the JAK2/STAT3 pathway in ovarian cancer results in the loss of cancer stem cell-like characteristics and a reduced tumor burden. *BMC Cancer*. 14:317. <https://doi.org/10.1186/1471-2407-14-317>
- AlHossiny, M., L. Luo, W.R. Frazier, N. Steiner, Y. Gusev, B. Kallakury, E. Glasgow, K. Creswell, S. Madhavan, R. Kumar, and G. Upadhyay. 2016. Ly6E/K signaling to TGF β promotes breast cancer progression, immune escape, and drug resistance. *Cancer Res*. 76:3376–3386. <https://doi.org/10.1158/0008-5472.CAN-15-2654>
- Bapat, S.A., A.M. Mali, C.B. Koppikar, and N.K. Kurrey. 2005. Stem and progenitor-like cells contribute to the aggressive behavior of human epithelial ovarian cancer. *Cancer Res*. 65:3025–3029. <https://doi.org/10.1158/0008-5472.CAN-04-3931>
- Baratin, M., L. Simon, A. Jorquera, C. Clément, D. Dembele, J. Nowak, R. Gentek, S. Weinert, F. Klauschen, B. Malissen, et al. 2017. T Cell Zone Resident Macrophages Silently Dispose of Apoptotic Cells in the Lymph Node. *Immunity*. 47:349–362. <https://doi.org/10.1016/j.immuni.2017.07.019>
- Bénézech, C., N.-T. Luu, J.A. Walker, A.A. Kruglov, Y. Loo, K. Nakamura, Y. Zhang, S. Nayar, L.H. Jones, A. Flores-Langarica, et al. 2015. Inflammation-induced formation of fat-associated lymphoid clusters. *Nat. Immunol*. 16:819–828. <https://doi.org/10.1038/ni.3215>
- Bushnell, B. 2014. BBMap: A Fast, Accurate, Splice-Aware Aligner. Lawrence Berkeley National Laboratory, Berkeley, CA.
- Chakarov, S., H.Y. Lim, L. Tan, S.Y. Lim, P. See, J. Lum, X.-M. Zhang, S. Foo, S. Nakamizo, K. Duan, et al. 2019. Two distinct interstitial macrophage populations coexist across tissues in specific subtissular niches. *Science*. 363:eaa0964. <https://doi.org/10.1126/science.aau0964>
- Chakrabarti, R., T. Celià-Terrassa, S. Kumar, X. Hang, Y. Wei, A. Choudhury, J. Hwang, J. Peng, B. Nixon, J.J. Grady, et al. 2018. Notch ligand Dll1 mediates cross-talk between mammary stem cells and the macrophageal niche. *Science*. 360:eaan4153. <https://doi.org/10.1126/science.aan4153>
- Charles, K.A., H. Kulbe, R. Soper, M. Escorcio-Correia, T. Lawrence, A. Schultheis, P. Chakravarty, R.G. Thompson, G. Kollias, J.F. Smyth, et al. 2009. The tumor-promoting actions of TNF- α involve TNFR1 and IL-17 in ovarian cancer in mice and humans. *J. Clin. Invest*. 119:3011–3023. <https://doi.org/10.1172/JCI39065>
- Chen, J., P. Ding, L. Li, H. Gu, X. Zhang, L. Zhang, N. Wang, L. Gan, Q. Wang, W. Zhang, and W. Hu. 2017. CD59 regulation by SOX2 is required for epithelial cancer stem cells to evade complement surveillance. *Stem Cell Reports*. 8:140–151. <https://doi.org/10.1016/j.stemcr.2016.11.008>
- Chou, J., S. Provot, and Z. Werb. 2010. GATA3 in development and cancer differentiation: cells GATA have it! *J. Cell. Physiol*. 222:42–49. <https://doi.org/10.1002/jcp.21943>
- Clark, R., V. Krishnan, M. Schoof, I. Rodriguez, B. Theriault, M. Chekmareva, and C. Rinker-Schaeffer. 2013. Milky spots promote ovarian cancer metastatic colonization of peritoneal adipose in experimental models. *Am. J. Pathol*. 183:576–591. <https://doi.org/10.1016/j.ajpath.2013.04.023>
- De Schepper, S., S. Verheijden, J. Aguilera-Lizarraga, M.F. Viola, W. Boesmans, N. Stakenborg, I. Voytyuk, I. Schmidt, B. Boeckx, I. Dierckx de Casterlé, et al. 2018. Self-maintaining gut macrophages are essential for intestinal homeostasis. *Cell*. 175:400–415.e13. <https://doi.org/10.1016/j.cell.2018.07.048>
- Dick, S.A., J.A. Macklin, S. Nejat, A. Momen, X. Clemente-Casares, M.G. Althagafi, J. Chen, C. Kantores, S. Hosseinzadeh, L. Aronoff, et al. 2019. Self-renewing resident cardiac macrophages limit adverse remodeling following myocardial infarction. *Nat. Immunol*. 20:29–39. <https://doi.org/10.1038/s41590-018-0272-2>
- Dobin, A., C.A. Davis, F. Schlesinger, J. Drenkow, C. Zaleski, S. Jha, P. Batut, M. Chaisson, and T.R. Gingeras. 2013. STAR: ultrafast universal RNA-seq aligner. *Bioinformatics*. 29:15–21. <https://doi.org/10.1093/bioinformatics/bts635>
- Etzerodt, A., and S.K. Moestrup. 2013. CD163 and inflammation: biological, diagnostic, and therapeutic aspects. *Antioxid. Redox Signal*. 18:2352–2363. <https://doi.org/10.1089/ars.2012.4834>
- Etzerodt, A., M.B. Maniecki, J.H. Graversen, H.J. Møller, V.P. Torchilin, and S.K. Moestrup. 2012. Efficient intracellular drug-targeting of macrophages using stealth liposomes directed to the hemoglobin scavenger receptor CD163. *J. Control. Release*. 160:72–80. <https://doi.org/10.1016/j.jconrel.2012.01.034>
- Etzerodt, A., M. Kjolby, M.J. Nielsen, M. Maniecki, P. Svendsen, and S.K. Moestrup. 2013. Plasma clearance of hemoglobin and haptoglobin in mice and effect of CD163 gene targeting disruption. *Antioxid. Redox Signal*. 18:2254–2263. <https://doi.org/10.1089/ars.2012.4605>
- Etzerodt, A., K. Tsalkitzi, M. Maniecki, W. Damsky, M. Delfini, E. Baudoin, M. Moulin, M. Bosenberg, J.H. Graversen, N. Auphan-Anezin, et al. 2019. Specific targeting of CD163⁺ TAMs mobilizes inflammatory monocytes and promotes T cell-mediated tumor regression. *J. Exp. Med*. 216:2394–2411. <https://doi.org/10.1084/jem.20182124>
- Ferlay, J., M. Ervik, F. Lam, M. Colombet, L. Mery, M. Piñeros, A. Znaor, I. Soerjomataram, and F. Bray. 2018. Global Cancer Observatory: Cancer Today. International Agency for Research on Cancer, Lyon, France. Available at: <https://gco.iarc.fr/today>.
- Ford, C.E., G. Punnia-Moorthy, C.E. Henry, E. Llamosas, S. Nixdorf, J. Olivier, R. Caduff, R.L. Ward, and V. Heinzelmann-Schwarz. 2014. The non-canonical Wnt ligand, Wnt5a, is upregulated and associated with epithelial to mesenchymal transition in epithelial ovarian cancer. *Gynecol. Oncol*. 134:338–345. <https://doi.org/10.1016/j.ygyno.2014.06.004>
- Fritze, A., F. Hens, A. Kimpfler, R. Schubert, and R. Peschka-Süss. 2006. Remote loading of doxorubicin into liposomes driven by a transmembrane phosphate gradient. *Biochimica et Biophysica Acta*. 1758:1633–1640. <https://doi.org/10.1016/j.bbamem.2006.05.028>
- Garson, K., and B.C. Vanderhyden. 2015. Epithelial ovarian cancer stem cells: underlying complexity of a simple paradigm. *Reproduction*. 149:R59–R70. <https://doi.org/10.1530/REP-14-0234>
- Ginhoux, F., and M. Guillemin. 2016. Tissue-resident macrophage ontogeny and homeostasis. *Immunity*. 44:439–449. <https://doi.org/10.1016/j.immuni.2016.02.024>
- Ginhoux, F., and M. Merad. 2010. Ontogeny and homeostasis of Langerhans cells. *Immunol. Cell Biol*. 88:387–392. <https://doi.org/10.1038/icb.2010.38>
- Ginhoux, F., M. Greter, M. Leboeuf, S. Nandi, P. See, S. Gokhan, M.F. Mehler, S.J. Conway, L.G. Ng, E.R. Stanley, et al. 2010. Fate mapping analysis reveals that adult microglia derive from primitive macrophages. *Science*. 330:841–845. <https://doi.org/10.1126/science.1194637>
- Goossens, P., J. Rodriguez-Vita, A. Etzerodt, M. Masse, O. Rastoin, V. Gouirand, T. Ulas, O. Papantonopoulou, M. Van Eck, N. Auphan-Anezin, et al. 2019. Membrane cholesterol efflux drives tumor-associated macrophage reprogramming and tumor progression. *Cell Metab*. 29:1376–1389.e4. <https://doi.org/10.1016/j.cmet.2019.02.016>
- Gray, E.E., and J.G. Cyster. 2012. Lymph node macrophages. *J. Innate Immun*. 4:424–436. <https://doi.org/10.1159/000337007>
- Hafemeister, C., and R. Satija. 2019. Normalization and variance stabilization of single-cell RNA-seq data using regularized negative binomial regression. *Genome Biology*. 20. 296. <https://doi.org/10.1186/s13059-019-1874-1>
- Hagemann, T., T. Lawrence, I. McNeish, K.A. Charles, H. Kulbe, R.G. Thompson, S.C. Robinson, and F.R. Balkwill. 2008. “Re-educating” tumor-associated macrophages by targeting NF- κ B. *J. Exp. Med*. 205:1261–1268. <https://doi.org/10.1084/jem.20080108>
- Hagiwara, A., T. Takahashi, K. Sawai, H. Taniguchi, M. Shimotsuma, S. Okano, C. Sakakura, H. Tsujimoto, K. Osaki, S. Sasaki, et al. 1993. Milky spots as the implantation site for malignant cells in peritoneal dissemination in mice. *Cancer Res*. 53:687–692.
- Hansen, K.D., R.A. Irizarry, and Z. Wu. 2012. Removing technical variability in RNA-seq data using conditional quantile normalization. *Biostatistics*. 13:204–216. <https://doi.org/10.1093/biostatistics/kxr054>
- Jäppinen, N., I. Félix, E. Lokka, S. Tyystjärvi, A. Pynttari, T. Lahtela, H. Gerke, K. Elima, P. Rantakari, and M. Salmi. 2019. Fetal-derived macrophages dominate in adult mammary glands. *Nat. Commun*. 10:281. <https://doi.org/10.1038/s41467-018-08065-1>
- Jung, Y., A.M. Decker, J. Wang, E. Lee, L.A. Kana, K. Yumoto, F.C. Cackowski, J. Rhee, P. Carmeliet, L. Buttitta, et al. 2016. Endogenous GAS6 and Mer receptor signaling regulate prostate cancer stem cells in bone marrow. *Oncotarget*. 7:25698–25711. <https://doi.org/10.18632/oncotarget.8365>
- Kim, D., B.-H. Choi, I.-G. Ryoo, and M.-K. Kwak. 2018. High NRF2 level mediates cancer stem cell-like properties of aldehyde dehydrogenase (ALDH)-high ovarian cancer cells: inhibitory role of all-trans retinoic acid in ALDH/NRF2 signaling. *Cell Death Dis*. 9:896. <https://doi.org/10.1038/s41419-018-0903-4>

- Kipps, E., D.S.P. Tan, and S.B. Kaye. 2013. Meeting the challenge of ascites in ovarian cancer: new avenues for therapy and research. *Nat. Rev. Cancer*. 13:273–282. <https://doi.org/10.1038/nrc3432>
- Komohara, Y., M. Jinushi, and M. Takeya. 2014. Clinical significance of macrophage heterogeneity in human malignant tumors. *Cancer Sci*. 105: 1–8. <https://doi.org/10.1111/cas.12314>
- Kreso, A., and J.E. Dick. 2014. Evolution of the cancer stem cell model. *Cell Stem Cell*. 14:275–291. <https://doi.org/10.1016/j.stem.2014.02.006>
- Krist, L.F.G., I.L. Eestermans, J.J.E. Steenberg, E.C.M. Hoefsmid, M.A. Cuesta, S. Meyer, and R.H.J. Beelen. 1995. Cellular composition of milky spots in the human greater omentum: an immunohistochemical and ultrastructural study. *Anat. Rec.* 241:163–174. <https://doi.org/10.1002/ar.1092410204>
- Lahmar, Q., J. Keirsse, D. Laoui, K. Movahedi, E. Van Overmeire, and J.A. Van Ginderachter. 2016. Tissue-resident versus monocyte-derived macrophages in the tumor microenvironment. *Biochim. Biophys. Acta*. 1865: 23–34. <https://doi.org/10.1016/j.bbcan.2015.06.009>
- Lee, K.-M., W. Han, J.B. Kim, I. Shin, E. Ko, I.A. Park, D.S. Lee, K. Oh, and D.-Y. Noh. 2012. The CD49d⁺/high subpopulation from isolated human breast sarcoma spheres possesses tumor-initiating ability. *Int. J. Oncol.* 40: 665–672. <https://doi.org/10.3892/ijo.2011.1289>
- Lee, C.-C., J.-C. Lin, W.-L. Hwang, Y.-J. Kuo, H.-K. Chen, S.-K. Tai, C.-C. Lin, and M.-H. Yang. 2018. Macrophage-secreted interleukin-35 regulates cancer cell plasticity to facilitate metastatic colonization. *Nat. Commun.* 9:3763. <https://doi.org/10.1038/s41467-018-06268-0>
- Lee, W., S.Y. Ko, M.S. Mohamed, H.A. Kenny, E. Lengyel, and H. Naora. 2019. Neutrophils facilitate ovarian cancer premetastatic niche formation in the omentum. *J. Exp. Med.* 216:176–194. <https://doi.org/10.1084/jem.20181170>
- Lengyel, E. 2010. Ovarian cancer development and metastasis. *Am. J. Pathol.* 177:1053–1064. <https://doi.org/10.2353/ajpath.2010.100105>
- Levin, T.G., A.E. Powell, P.S. Davies, A.D. Silk, A.D. Dismuke, E.C. Anderson, J.R. Swain, and M.H. Wong. 2010. Characterization of the intestinal cancer stem cell marker CD166 in the human and mouse gastrointestinal tract. *Gastroenterology*. 139:2072–2082.e5. <https://doi.org/10.1053/j.gastro.2010.08.053>
- Levina, V.V., B. Nolen, Y. Su, A.K. Godwin, D. Fishman, J. Liu, G. Mor, L.G. Maxwell, R.B. Herberman, M.J. Szczepanski, et al. 2009. Biological significance of prolactin in gynecological cancers. *Cancer Res*. 69: 5226–5233. <https://doi.org/10.1158/0008-5472.CAN-08-4652>
- Lim, H.Y., S.Y. Lim, C.K. Tan, C.H. Thiam, C.C. Goh, D. Carbajo, S.H.S. Chew, P. See, S. Chakarov, X.N. Wang, et al. 2018. Hyaluronan receptor LYVE-1-expressing macrophages maintain arterial tone through hyaluronan-mediated regulation of smooth muscle cell collagen. *Immunity*. 49: 326–341.e7. <https://doi.org/10.1016/j.immuni.2018.06.008>
- Love, M.I., W. Huber, and S. Anders. 2014. Moderated estimation of fold change and dispersion for RNA-seq data with DESeq2. *Genome Biol.* 15: 550. <https://doi.org/10.1186/s13059-014-0550-8>
- Loyer, P.-L., P. Hamon, M. Laviron, A. Meghraoui-Kheddar, E. Goncalves, Z. Deng, S. Torstensson, N. Bercovici, C. Baudesson de Chanville, B. Combadière, et al. 2018. Macrophages of distinct origins contribute to tumor development in the lung. *J. Exp. Med.* 215:2536–2553. <https://doi.org/10.1084/jem.20180534>
- Lupia, M., and U. Cavallaro. 2017. Ovarian cancer stem cells: still an elusive entity? *Mol. Cancer*. 16:64. <https://doi.org/10.1186/s12943-017-0638-3>
- Meng, E., A. Mitra, K. Tripathi, M.A. Finan, J. Scalici, S. McClellan, L. Madeira da Silva, E. Reed, L.A. Shevde, K. Palle, and R.P. Rocconi. 2014. ALDH1A1 maintains ovarian cancer stem cell-like properties by altered regulation of cell cycle checkpoint and DNA repair network signaling. *PLoS One*. 9: e107142. <https://doi.org/10.1371/journal.pone.0107142>
- Mossadegh-Keller, N., R. Gentek, G. Gimenez, S. Bigot, S. Mailfert, and M.H. Sieweke. 2017. Developmental origin and maintenance of distinct testicular macrophage populations. *J. Exp. Med.* 214:2829–2841. <https://doi.org/10.1084/jem.20170829>
- Motz, G.T., S.P. Santoro, L.-P. Wang, T. Garrabrant, R.R. Lastra, I.S. Hagemann, P. Lal, M.D. Feldman, F. Benencia, and G. Coukos. 2014. Tumor endothelium FasL establishes a selective immune barrier promoting tolerance in tumors. *Nat. Med.* 20:607–615. <https://doi.org/10.1038/nm.3541>
- Nieto, M.A., R.Y.-J. Huang, R.A. Jackson, and J.P. Thiery. 2016. EMT: 2016. *Cell*. 166:21–45. <https://doi.org/10.1016/j.cell.2016.06.028>
- Noy, R., and J.W. Pollard. 2014. Tumor-associated macrophages: from mechanisms to therapy. *Immunity*. 41:49–61. <https://doi.org/10.1016/j.immuni.2014.06.010>
- Ojalvo, L.S., C.A. Whittaker, J.S. Condeelis, and J.W. Pollard. 2010. Gene expression analysis of macrophages that facilitate tumor invasion supports a role for Wnt-signaling in mediating their activity in primary mammary tumors. *J. Immunol.* 184:702–712. <https://doi.org/10.4049/jimmunol.0902360>
- Oktem, G., O. Sercan, U. Guven, R. Uslu, A. Uysal, G. Goksel, S. Ayla, and A. Bilir. 2014. Cancer stem cell differentiation: TGFβ1 and versican may trigger molecules for the organization of tumor spheroids. *Oncol. Rep.* 32:641–649. <https://doi.org/10.3892/or.2014.3252>
- Parte, S.C., S.K. Batra, and S.S. Kakar. 2018. Characterization of stem cell and cancer stem cell populations in ovary and ovarian tumors. *J. Ovarian Res.* 11:69. <https://doi.org/10.1186/s13048-018-0439-3>
- Pattabiraman, D.R., and R.A. Weinberg. 2014. Tackling the cancer stem cells - what challenges do they pose? *Nat. Rev. Drug Discov.* 13:497–512. <https://doi.org/10.1038/nrd4253>
- Pearce, O.M.T., R.M. Delaine-Smith, E. Maniati, S. Nichols, J. Wang, S. Böhm, V. Rajeev, D. Ullah, P. Chakravarty, R.R. Jones, et al. 2018. Deconstruction of a metastatic tumor microenvironment reveals a common matrix response in human cancers. *Cancer Discov.* 8:304–319. <https://doi.org/10.1158/2159-8290.CD-17-0284>
- Pollard, J.W. 2009. Trophic macrophages in development and disease. *Nat. Rev. Immunol.* 9:259–270. <https://doi.org/10.1038/nri2528>
- Raggi, C., H.S. Mousa, M. Correnti, A. Sica, and P. Invernizzi. 2016. Cancer stem cells and tumor-associated macrophages: a roadmap for multi-targeting strategies. *Oncogene*. 35:671–682. <https://doi.org/10.1038/onc.2015.132>
- Rangel-Moreno, J., J.E. Moyron-Quiroz, D.M. Carragher, K. Kusser, L. Hartson, A. Moquin, and T.D. Randall. 2009. Omental milky spots develop in the absence of lymphoid tissue-inducer cells and support B and T cell responses to peritoneal antigens. *Immunity*. 30:731–743. <https://doi.org/10.1016/j.immuni.2009.03.014>
- Roby, K.F., C.C. Taylor, J.P. Sweetwood, Y. Cheng, J.L. Pace, O. Tawfik, D.L. Persons, P.G. Smith, and P.F. Terranova. 2000. Development of a syngeneic mouse model for events related to ovarian cancer. *Carcinogenesis*. 21:585–591. <https://doi.org/10.1093/carcin/21.4.585>
- Rosas, M., L.C. Davies, P.J. Giles, C.-T. Liao, B. Kharfan, T.C. Stone, V.B. O'Donnell, D.J. Fraser, S.A. Jones, and P.R. Taylor. 2014. The transcription factor Gata6 links tissue macrophage phenotype and proliferative renewal. *Science*. 344:645–648. <https://doi.org/10.1126/science.1251414>
- Saygin, C., A. Wiechert, V.S. Rao, R. Alluri, E. Connor, P.S. Thiagarajan, J.S. Hale, Y. Li, A. Chumakova, A. Jarrar, et al. 2017. CD55 regulates self-renewal and cisplatin resistance in endometrioid tumors. *J. Exp. Med.* 214:2715–2732. <https://doi.org/10.1084/jem.20170438>
- Schreiber, H.A., J. Loschko, R.A. Karssemeijer, A. Escolano, M.M. Meredith, D. Mucida, P. Guernonprez, and M.C. Nussenzweig. 2013. Intestinal monocytes and macrophages are required for T cell polarization in response to *Citrobacter rodentium*. *J. Exp. Med.* 210:2025–2039. <https://doi.org/10.1084/jem.20130903>
- Schulz, C., E. Gomez Perdiguero, L. Chorro, H. Szabo-Rogers, N. Cagnard, K. Kierdorf, M. Prinz, B. Wu, S.E.W. Jacobsen, J.W. Pollard, et al. 2012. A lineage of myeloid cells independent of Myb and hematopoietic stem cells. *Science*. 336:86–90. <https://doi.org/10.1126/science.1219179>
- Scott, C.L., F. Zheng, P. De Baetselier, L. Martens, Y. Saeys, S. De Prijck, S. Lippens, C. Abels, S. Schoonooghe, G. Raes, et al. 2016. Bone marrow-derived monocytes give rise to self-renewing and fully differentiated Kupffer cells. *Nat. Commun.* 7:10321. <https://doi.org/10.1038/ncomms10321>
- Sehoul, J., F. Senyuya, C. Fotopoulou, U. Neumann, C. Denkert, L. Werner, and O.Ö. Gülten. 2009. Intra-abdominal tumor dissemination pattern and surgical outcome in 214 patients with primary ovarian cancer. *J. Surg. Oncol.* 99:424–427. <https://doi.org/10.1002/jso.21288>
- Seo, E.J., Y.W. Kwon, I.H. Jang, D.K. Kim, S.I. Lee, E.J. Choi, K.H. Kim, D.S. Suh, J.H. Lee, K.U. Choi, et al. 2016. Autotaxin regulates maintenance of ovarian cancer stem cells through lysophosphatidic acid-mediated autocrine mechanism. *Stem Cells*. 34:551–564. <https://doi.org/10.1002/stem.2279>
- Solar, P., L. Feldman, J.Y. Jeong, J.R. Busingye, and A.J. Sytkowski. 2008. Erythropoietin treatment of human ovarian cancer cells results in enhanced signaling and a paclitaxel-resistant phenotype. *Int. J. Cancer*. 122: 281–288. <https://doi.org/10.1002/ijc.23071>
- Soucie, E.L., Z. Weng, L. Geirsdóttir, K. Molawi, J. Maurizio, R. Fenouil, N. Mossadegh-Keller, G. Gimenez, L. VanHille, M. Beniazza, et al. 2016. Lineage-specific enhancers activate self-renewal genes in macrophages

- and embryonic stem cells. *Science*. 351:aad5510. <https://doi.org/10.1126/science.aad5510>
- Steg, A.D., K.S. Bevis, A.A. Katre, A. Ziebarth, Z.C. Dobbin, R.D. Alvarez, K. Zhang, M. Conner, and C.N. Landen. 2012. Stem cell pathways contribute to clinical chemoresistance in ovarian cancer. *Clin. Cancer Res.* 18:869–881. <https://doi.org/10.1158/1078-0432.CCR-11-2188>
- Torchilin, V.P., T.S. Levchenko, A.N. Lukyanov, B.A. Khaw, A.L. Klibanov, R. Rammohan, G.P. Samokhin, and K.R. Whiteman. 2001. p-Nitrophenylcarbonyl-PEG-PE-liposomes: fast and simple attachment of specific ligands, including monoclonal antibodies, to distal ends of PEG chains via p-nitrophenylcarbonyl groups. *Biochim. Biophys. Acta.* 1511: 397–411. [https://doi.org/10.1016/S0005-2728\(01\)00165-7](https://doi.org/10.1016/S0005-2728(01)00165-7)
- Wang, Q.-E. 2015. DNA damage responses in cancer stem cells: Implications for cancer therapeutic strategies. *World J. Biol. Chem.* 6:57–64. <https://doi.org/10.4331/wjbc.v6.i3.57>
- Wang, E., S. Bhattacharyya, A. Szabolcs, C. Rodriguez-Aguayo, N.B. Jennings, G. Lopez-Berestein, P. Mukherjee, A.K. Sood, and R. Bhattacharya. 2011. Enhancing chemotherapy response with Bmi-1 silencing in ovarian cancer. *PLoS One*. 6:e17918. <https://doi.org/10.1371/journal.pone.0017918>
- Wang, Y., X. Zong, S. Mitra, A.K. Mitra, D. Matei, and K.P. Nephew. 2018. IL-6 mediates platinum-induced enrichment of ovarian cancer stem cells. *JCI Insight*. 3:122360. <https://doi.org/10.1172/jci.insight.122360>
- Wehrens, R., and L.M.C. Buydens. 2007. Self- and super-organizing maps in R: the kohonenpackage. *J. Stat. Softw.* 21:1–19. <https://doi.org/10.18637/jss.v021.i05>
- Wehrens, R., and J. Kruisselbrink. 2018. Flexible self-organizing maps in kohonen3.0. *J. Stat. Softw.* 87. <https://doi.org/10.18637/jss.v087.i07>
- Wei, L., F. Yin, W. Zhang, and L. Li. 2017. STROBE-compliant integrin through focal adhesion involve in cancer stem cell and multidrug resistance of ovarian cancer. *Medicine (Baltimore)*. 96:e6345. <https://doi.org/10.1097/MD.0000000000006345>
- Witt, A.E., C.-W. Lee, T.I. Lee, D.J. Azzam, B. Wang, C. Caslini, F. Petrocca, J. Grosso, M. Jones, E.B. Cohick, et al. 2017. Identification of a cancer stem cell-specific function for the histone deacetylases, HDAC1 and HDAC7, in breast and ovarian cancer. *Oncogene*. 36:1707–1720. <https://doi.org/10.1038/onc.2016.337>
- Yan, W., Q.J. Cao, R.B. Arenas, B. Bentley, and R. Shao. 2010. GATA3 inhibits breast cancer metastasis through the reversal of epithelial-mesenchymal transition. *J. Biol. Chem.* 285:14042–14051. <https://doi.org/10.1074/jbc.M110.105262>
- Yang, Z., L. He, K. Lin, Y. Zhang, A. Deng, Y. Liang, C. Li, and T. Wen. 2017. The KMT1A-GATA3-STAT3 circuit is a novel self-renewal signaling of human bladder cancer stem cells. *Clin. Cancer Res.* 23:6673–6685. <https://doi.org/10.1158/1078-0432.CCR-17-0882>
- Yang, M., D. McKay, J.W. Pollard, and C.E. Lewis. 2018. Diverse functions of macrophages in different tumor microenvironments. *Cancer Res.* 78: 5492–5503. <https://doi.org/10.1158/0008-5472.CAN-18-1367>
- Yasuda, K., Y. Hirohashi, T. Kuroda, A. Takaya, T. Kubo, T. Kanaseki, T. Tsukahara, T. Hasegawa, T. Saito, N. Sato, and T. Torigoe. 2016. MAPK13 is preferentially expressed in gynecological cancer stem cells and has a role in the tumor-initiation. *Biochem. Biophys. Res. Commun.* 472:643–647. <https://doi.org/10.1016/j.bbrc.2016.03.004>
- Yates, A., W. Akanni, M.R. Amode, D. Barrell, K. Billis, D. Carvalho-Silva, C. Cummins, P. Clapham, S. Fitzgerald, L. Gil, et al. 2016. Ensembl 2016. *Nucleic Acids Res.* 44(D1):D710–D716. <https://doi.org/10.1093/nar/gkv1157>
- Yona, S., K.-W. Kim, Y. Wolf, A. Mildner, D. Varol, M. Breker, D. Strauss-Ayali, S. Viukov, M. Guillems, A. Misharin, et al. 2013. Fate mapping reveals origins and dynamics of monocytes and tissue macrophages under homeostasis. *Immunity*. 38:79–91. <https://doi.org/10.1016/j.immuni.2012.12.001>
- Yu, G., L.-G. Wang, Y. Han, and Q.-Y. He. 2012. clusterProfiler: an R package for comparing biological themes among gene clusters. *OMICS*. 16: 284–287. <https://doi.org/10.1089/omi.2011.0118>
- Zhang, J., B. Yuan, H. Zhang, and H. Li. 2019. Human epithelial ovarian cancer cells expressing CD105, CD44 and CD106 surface markers exhibit increased invasive capacity and drug resistance. *Oncol. Lett.* 17: 5351–5360. <https://doi.org/10.3892/ol.2019.10221>
- Zhu, Y., J.M. Herndon, D.K. Sojka, K.-W. Kim, B.L. Knolhoff, C. Zuo, D.R. Cullinan, J. Luo, A.R. Bearden, K.J. Lavine, et al. 2017. Tissue-resident macrophages in pancreatic ductal adenocarcinoma originate from embryonic hematopoiesis and promote tumor progression. *Immunity*. 47: 323–338.e6. <https://doi.org/10.1016/j.immuni.2017.07.014>

Supplemental material

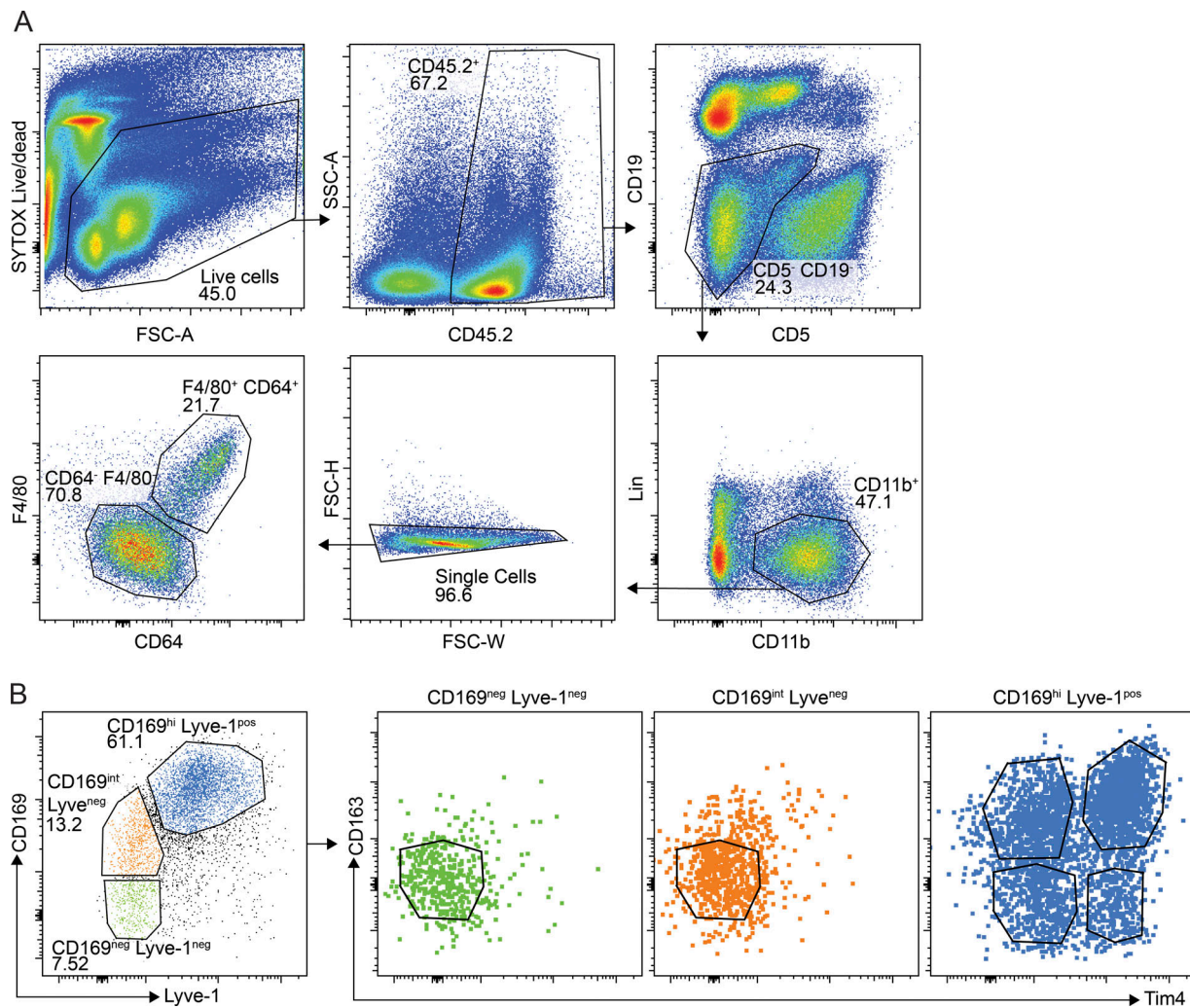


Figure S1. **Gating strategy and expression of Tim4 and CD163 on omental macrophages. (A)** Gating strategy for the myeloid cell compartment excluding neutrophils. Myeloid cells were gated as Live (forward scatter area [FSC-A] versus Sytox Blue), CD45.2⁺ (CD45.2 versus SSC-A), CD5⁻, CD19⁻ (CD5 versus CD19), Lin^{neg}(NK1.1, Ly6G), CD11b⁺ (CD11b versus Lineage), single cells (forward scatter height [FSC-H] versus forward scatter width [FSC-W]), and CD64⁺ and F4/80⁺ (F4/80 versus CD64). **(B)** Expression of CD163 and Tim4 among F4/80⁺ CD64⁺ macrophages that are CD169^{neg}Lyve-1^{neg} (green), CD169^{int} Lyve-1^{neg} (red), or CD169^{hi} Lyve-1^{pos} (blue). Data are representative of two independent experiments.

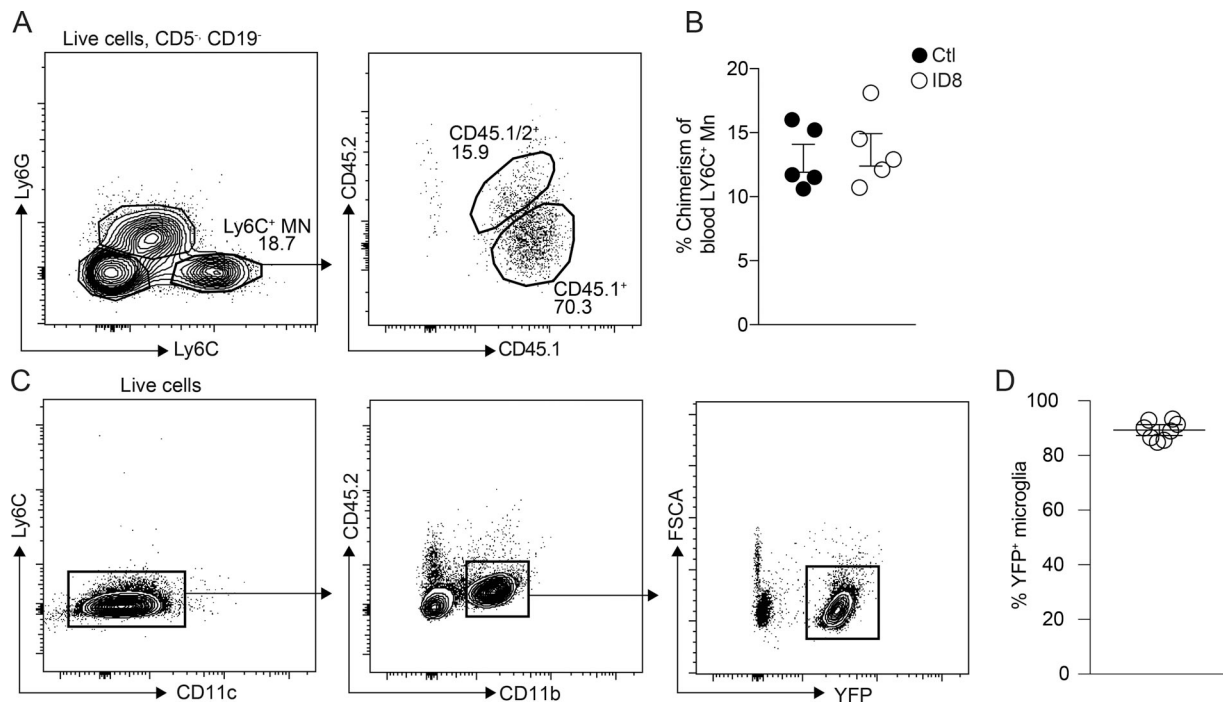


Figure S2. **Fate mapping of omental macrophages.** (A and B) Flow cytometric analysis of blood monocytes in mice 5 wk (A) or 13 wk (B) after adoptive transfer of CD45.1⁺/CD45.2⁺ donor bone marrow in irradiated CD45.1⁺ host mice that were protected by a lead shield. Monocytes were gated as Live (FSC-A versus Sytox Blue), CD5^{neg}, CD19^{neg} (CD5 versus CD19), NK1.1^{neg}, CD11b⁺ (CD11b versus NK1.1), and Ly6C⁺, Ly6G^{neg} (Ly6C versus Ly6G). Data are represented as mean \pm SEM of $n = 5$. (C) Flow cytometric analysis of YFP⁺ microglia in Cx3Cr1CreER:R26-yfp mice pulse-labeled with tamoxifen at E16.5. Microglia were gated as Live (FSC-A versus Sytox Blue), Ly6C^{neg}, CD11c^{neg} (Ly6C versus CD11c), and CD45.2^{dim}, CD11b^{hi} (CD11b versus CD45.2). Data are represented as mean \pm SEM of $n = 6$. All data are representative of two independent experiments.

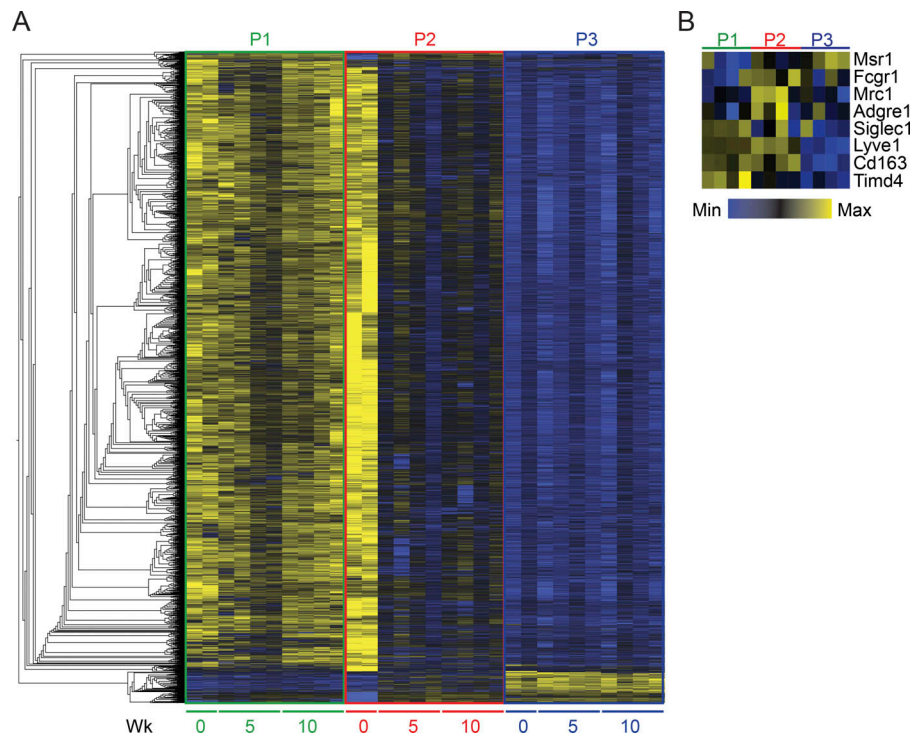


Figure S3. **Hierarchical clustering analysis of omental macrophages.** **(A)** Heatmap showing hierarchical clustering analysis of the 5,000 most DEGs in P1 (green), P2 (red), and P3 (blue) CD169^{hi} Lyve-1^{pos} omental macrophages sorted at steady state (0 wk) or 5 wk and 10 wk after infiltration of ID8 ovarian cancer cells. **(B)** Heatmap showing expression of macrophage markers from transcriptomic analysis of P1 (green), P2 (red), and P3 (blue) CD169^{hi} Lyve-1^{pos} omental macrophages sorted 10 wk after ID8 injection (Fig. 2 E). Libraries were prepared from two independent experiments with $n = 2$ and sequenced on the same flow cell for a total of four biological replicates.

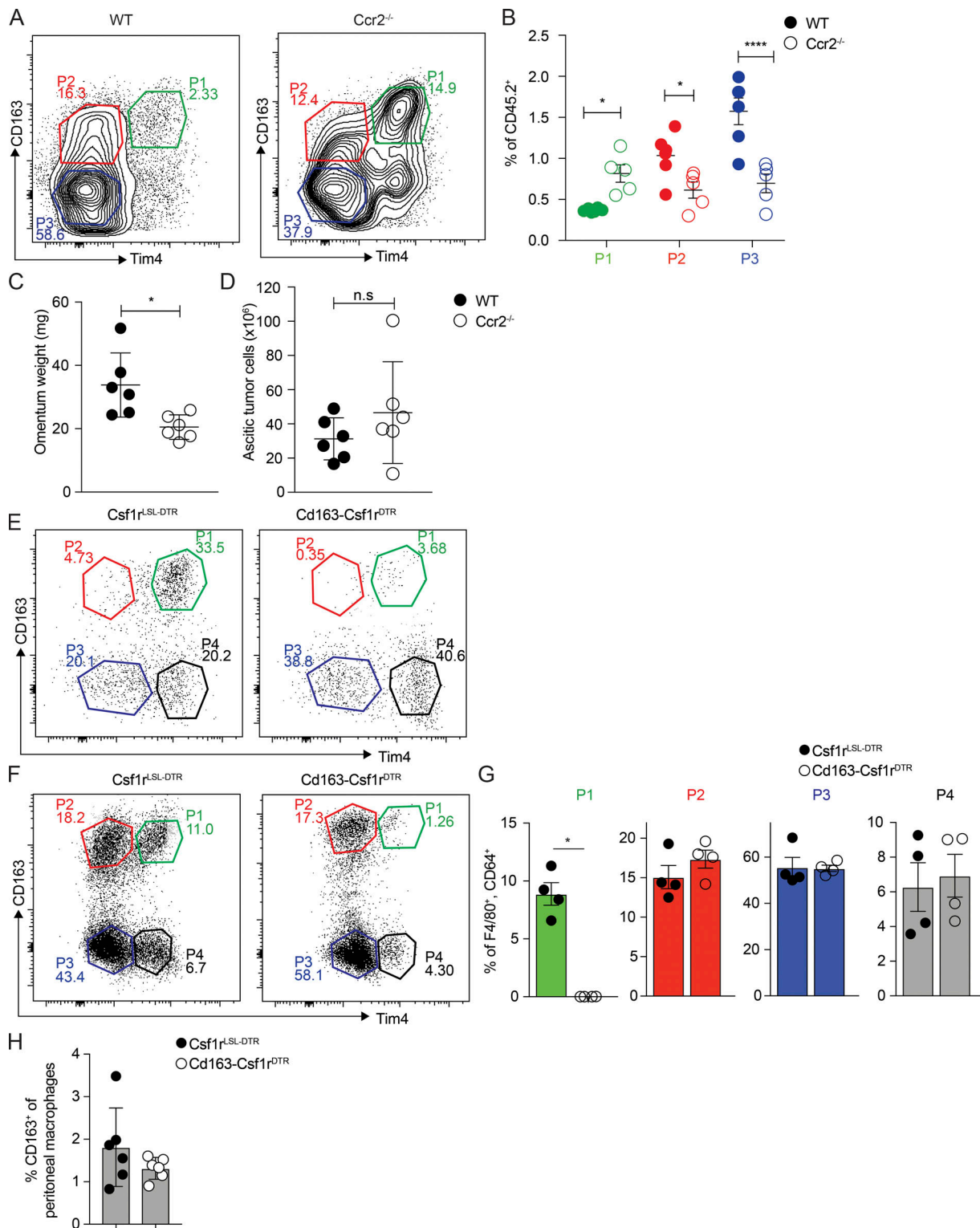


Figure S4. **Depletion of monocyte-derived and tissue-resident omental macrophages.** (A and B) Flow cytometric analysis of CD169^{hi} Lyve-1^{pos} omental macrophages in *Ccr2*^{-/-} mice 10 wk after i.p. injection of 106 ID8 ovarian cancer cells. Data are represented as mean ± SEM of *n* = 5, and statistically significant difference was calculated using two-way ANOVA followed by Tukey post hoc test; *, *P* < 0.05; ****, *P* < 0.0001. (C and D) Omentum weight (C) and number of tumor cells in ascites (D) of WT and *Ccr2*^{-/-} mice 10 wk after injection of ID8 cells. Data are represented as mean ± SEM of *n* = 6, and statistically significant difference was calculated using Mann-Whitney *U* test; *, *P* < 0.05. (E–G) Flow cytometric analysis of CD169^{hi} Lyve-1^{pos} omental macrophages in *Cd163-Csf1r^{DTR}* mice 1 d (E) or 6 d (F and G) after i.p. injection of 4 ng/kg DT. CD169^{hi} Lyve-1^{pos} omental macrophages were gated as described in Fig. S1A. (H) Flow cytometric analysis of peritoneal macrophages in *Cd163-Csf1r^{DTR}* and control mice 6 d after i.p. injection of 4 ng/kg DT. Peritoneal macrophages were gated as Live, CD45.2^{pos}, Lin^{neg}(CD5, CD19, Ly6G, NK1.1) CD11b⁺, F4/80⁺, and MHCII^{neg}. Data are represented as mean ± SEM of *n* = 7, and statistically significant difference was calculated using Mann-Whitney *U* test; *, *P* < 0.05. All data are representative of two independent experiments.

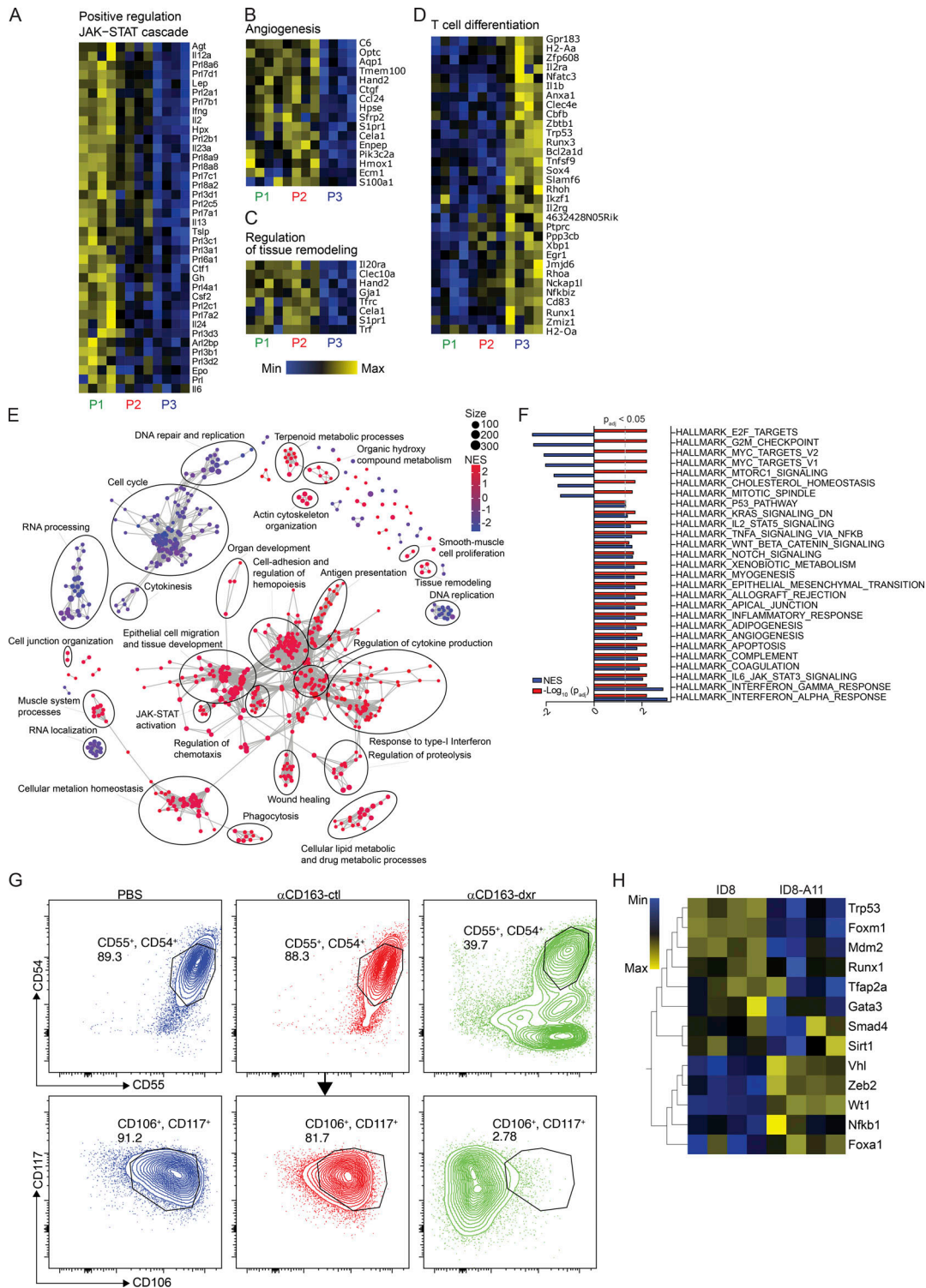


Figure S5. Transcriptomic analysis of ID8 ovarian cancer cells and TAMs from omentum. (A–D) Heatmaps showing expression of genes associated with the enriched pathways in Fig. 5 E: Positive regulation of JAK-STAT (A), angiogenesis (B), regulation of tissue remodeling (C), and T cell differentiation (D). **(E)** GO term enrichment analysis of RNAseq data comparing cultured ID8 cells ($n = 4$) and ID8 cells harvested from ascites 11 wk after transplantation in vivo (ID8-A11, $n = 4$). Identified GO terms are represented by nodes with a size according to the number of enriched genes. Nodes are colored according to the normalized enrichment score (NES). **(F)** GSEA comparing ID8 and ID8-A11 against the hallmark gene sets in MSigDB. **(G)** Flow cytometric analysis of CSC markers CD54, CD55, CD106, and CD117 on tumor cells from ascites of mice specifically depleted of Tim4⁺ CD163⁺ resident TAM (α CD163-dxr). Mice were injected i.p. with 1 mg/kg α CD163-dxr or controls (empty α CD163-LNP or PBS) on days 1, 3, and 5, before injection of ID8-Luc cells i.p. on day 8. 10 wk after ID8, tumor cells in ascites were harvested and analyzed for CSC marker expression by flow cytometry by gating on Live, CD45.2^{neg}, and Lin^{neg}(CD11b, F4/80, CD5, CD19, Ly6G, NK1.1) cells. **(H)** Heatmap showing expression levels of TFs involved in EMT and MET in ID8 and ID8-A11 cells. All data are representative of three independent experiments.

Table S1 is provided online as a separate Word file and lists markers associated with CSC phenotype in ovarian cancer.